FERMILAB-Pub-04/165-E August 2004

arXiv:hep-ex/0406002 v1 1 Jun 2004

Measurements of K_L Branching Fractions and the CP Violation Parameter $|\eta_{+-}|$

T. Alexopoulos,[11] M. Arenton,[10] R.F. Barbosa,[7,*] A.R. Barker,[5,†] L. Bellantoni,[7] A. Bellavance,[9] E. Blucher,[4] G.J. Bock,[7] E. Cheu,[1] S. Childress,[7] R. Coleman,[7] M.D. Corcoran,[9] B. Cox,[10] A.R. Erwin,[11] R. Ford,[7] A. Glazov,[4] A. Golossanov,[10] J. Graham,[4] J. Hamm,[1] K. Hanagaki,[8] Y.B. Hsiung,[7] H. Huang,[5] V. Jejer,[10] D.A. Jensen,[7] R. Kessler,[4] H.G.E. Kobrak,[3] K. Kotera,[8] J. LaDue,[5] A. Ledovskoy,[10] P.L. McBride,[7] E. Monnier,[4,‡] H. Nguyen,[7] R. Niclasen,[5] V. Prasad,[4] X.R. Qi,[7] E.J. Ramberg,[7] R.E. Ray,[7] M. Ronquest,[10] E. Santos,[7,*] P. Shanahan,[7] J. Shields,[10] W. Slater,[2] D. Smith,[10] N. Solomey,[4] E.C. Swallow,[4,6] P.A. Toale,[5] R. Tschirhart,[7] Y.W. Wah,[4] J. Wang,[1] H.B. White,[7] J. Whitmore,[7] M. Wilking,[5] B. Winstein,[4] R. Winston,[4] E.T. Worcester,[4] T. Yamanaka,[8] and E. D. Zimmerman[5]

(The KTeV Collaboration)

[1] *University of Arizona, Tucson, Arizona 85721*
[2] *University of California at Los Angeles, Los Angeles, California 90095*
[3] *University of California at San Diego, La Jolla, California 92093*
[4] *The Enrico Fermi Institute, The University of Chicago, Chicago, Illinois 60637*
[5] *University of Colorado, Boulder, Colorado 80309*
[6] *Elmhurst College, Elmhurst, Illinois 60126*
[7] *Fermi National Accelerator Laboratory, Batavia, Illinois 60510*
[8] *Osaka University, Toyonaka, Osaka 560-0043 Japan*
[9] *Rice University, Houston, Texas 77005*
[10] *The Department of Physics and Institute of Nuclear and Particle Physics, University of Virginia, Charlottesville, Virginia 22901*
[11] *University of Wisconsin, Madison, Wisconsin 53706*

We present new measurements of the six largest branching fractions of the K_L using data collected in 1997 by the KTeV experiment (E832) at Fermilab. The results are $B(K_L \to \pi^\pm e^\mp \nu) = 0.4067 \pm 0.0011$, $B(K_L \to \pi^\pm \mu^\mp \nu) = 0.2701 \pm 0.0009$, $B(K_L \to \pi^+\pi^-\pi^0) = 0.1252 \pm 0.0007$, $B(K_L \to \pi^0\pi^0\pi^0) = 0.1945 \pm 0.0018$, $B(K_L \to \pi^+\pi^-) = (1.975 \pm 0.012) \times 10^{-3}$, and $B(K_L \to \pi^0\pi^0) = (0.865 \pm 0.010) \times 10^{-3}$, where statistical and systematic errors have been summed in quadrature. We also determine the CP violation parameter $|\eta_{+-}|$ to be $(2.228 \pm 0.010) \times 10^{-3}$. Several of these results are not in good agreement with averages of previous measurements.

PACS numbers: 13.25.Es, 13.20.Eb

I. INTRODUCTION

Most recent experimental work on the K_L has focused on rare and CP violating decays. The branching fractions of the main K_L decay modes, however, have not been measured together in a modern, high-statistics experiment. These branching fractions are fundamental experimental parameters used to determine the CKM element $|V_{us}|$, the CP violation parameter $|\eta_{+-}|$, and the normalization for many other rare decay measurements.

In this paper, we present new results for the six largest K_L branching fractions: $K_L \to \pi^\pm e^\mp \nu$, $K_L \to \pi^\pm \mu^\mp \nu$, $K_L \to \pi^+\pi^-\pi^0$, $K_L \to \pi^0\pi^0\pi^0$, $K_L \to \pi^+\pi^-$, and $K_L \to \pi^0\pi^0$. We determine these branching fractions by measuring the following ratios of decay rates:

$$\Gamma_{K\mu3}/\Gamma_{Ke3} \equiv \Gamma(K_L \to \pi^\pm\mu^\mp\nu)/\Gamma(K_L \to \pi^\pm e^\mp \nu) \quad (1)$$
$$\Gamma_{+-0}/\Gamma_{Ke3} \equiv \Gamma(K_L \to \pi^+\pi^-\pi^0)/\Gamma(K_L \to \pi^\pm e^\mp \nu) \quad (2)$$
$$\Gamma_{000}/\Gamma_{Ke3} \equiv \Gamma(K_L \to \pi^0\pi^0\pi^0)/\Gamma(K_L \to \pi^\pm e^\mp \nu) \quad (3)$$
$$\Gamma_{+-}/\Gamma_{Ke3} \equiv \Gamma(K_L \to \pi^+\pi^-)/\Gamma(K_L \to \pi^\pm e^\mp \nu) \quad (4)$$
$$\Gamma_{00}/\Gamma_{000} \equiv \Gamma(K_L \to \pi^0\pi^0)/\Gamma(K_L \to \pi^0\pi^0\pi^0). \quad (5)$$

Each ratio is measured in a statistically independent data sample collected by the KTeV (E832) experiment at Fermilab. Note that throughout this paper, inner bremsstrahlung contributions are included for all decay modes with charged particles.

Since the six decay modes listed above account for more than 99.9% of the total decay rate, the five partial width ratios may be converted into branching fraction measurements. For example, the $K_L \to \pi^\pm e^\mp \nu$ branch-

*Permanent address: University of São Paulo, São Paulo, Brazil
†Deceased.
‡Permanent address: C.P.P. Marseille/C.N.R.S., France

ing fraction, B_{Ke3}, may be written as

$$B_{Ke3} = \frac{1 - B_{rare}}{1 + \frac{\Gamma_{K\mu3}}{\Gamma_{Ke3}} + \frac{\Gamma_{000}}{\Gamma_{Ke3}} + \frac{\Gamma_{+-0}}{\Gamma_{Ke3}} + \frac{\Gamma_{+-}}{\Gamma_{Ke3}} + \frac{\Gamma_{00}}{\Gamma_{Ke3}}}, \tag{6}$$

where $B_{rare} = 0.07\%$ is the sum of branching fractions of other rare K_L decay modes [40]. In terms of our measured partial width ratios, $\Gamma_{00}/\Gamma_{Ke3} = \Gamma_{00}/\Gamma_{000} \times \Gamma_{000}/\Gamma_{Ke3}$.

The paper is organized as follows. First, we give a brief description of the KTeV detector and the data sets used in this analysis. Next, we present an overview of the analysis techniques followed by a more detailed discussion of selection criteria for the individual decay modes. Section VII contains a description of the Monte Carlo simulation used to determine the detector acceptance, and a discussion of the resulting systematic uncertainties. In Section VIII, we present results for the partial width ratios and branching fractions, along with several crosschecks of our analysis. Our branching fraction measurements are then used to extract $|\eta_{+-}|$. Finally, our results are compared with previous measurements.

II. KTEV DETECTOR

The KTeV detector (see Fig. 1) and associated event reconstruction techniques have been described in detail elsewhere [1]. Here we give a brief summary of the essential detector components. An 800 GeV/c proton beam striking a BeO target is used to produce two almost parallel neutral beams, shaped by a series of collimators. Except for a special "low-intensity" run described later, a fully-active regenerator is placed in one of the beams to provide a source of K_S for the measurement of ϵ'/ϵ; decays in the "regenerator" beam are not used in this analysis. The other beam, referred to as the vacuum beam, provides K_L decays used for these measurements. A large vacuum decay region extends to 159 m from the primary target.

Following a thin vacuum window at the end of the vacuum region is a drift chamber spectrometer used to measure the momentum of charged particles; this spectrometer consists of four chambers, two upstream (DC1-DC2) and two downstream (DC3-DC4) of an analysis magnet that imparts a 0.41 GeV/c momentum kick in the horizontal plane. Each chamber measures positions in both the x and y views (transverse to the beam direction). Farther downstream lies a trigger (scintillator) hodoscope to identify charged particles, and a 3100 crystal, pure cesium iodide (CsI) electromagnetic calorimeter. Downstream of the CsI calorimeter there is a muon system consisting of scintillator hodoscopes behind 4 m and 5 m of steel. Veto detectors surround the vacuum decay region, each drift chamber, and the CsI calorimeter (Vacuum-Veto, Spec-Veto, and CsI-Veto).

KTeV uses a three-level trigger system to reduce the total rate of recorded events. The Level 1 and Level 2 triggers are implemented in hardware and the Level 3 trigger is a software filter that uses the full event reconstruction. With the exception of $K_L \to \pi^0\pi^0$, the data samples used in this analysis do not require the Level 3 trigger.

The analysis of the K_L branching fractions benefits from the KTeV detector design that was optimized to measure the direct CP violation parameter using a Monte Carlo simulation (MC) to determine the detector acceptance. To reduce uncertainties in the simulation, it is important that apertures and detector geometry are well measured, and that there is very little material before the calorimeter to affect decay products.

The Z-locations of detector elements are known with 100 μm precision. The transverse sizes of the drift chambers are known to 20 μm; the transverse dimensions and relative locations of the other detector elements are determined to better than 200 μm using charged particle tracks.

The detector has very little material upstream of the calorimeter, reducing losses from multiple scattering, hadronic interactions, and $\gamma \to e^+e^-$ conversions. The material from the vacuum window to the last drift chamber is only 0.012 radiation lengths (X_0), or 0.007 pion interaction length (Λ_0); the material downstream of the last drift chamber to the front face of the CsI is 0.031 X_0, or 0.014 Λ_0.

The analysis presented in this paper also benefits from extensive detector calibration performed for the ϵ'/ϵ analysis [1]. The momentum kick of the analysis magnet is determined to 0.01% precision using $K_L \to \pi^+\pi^-$ events and the PDG value of the kaon mass [2]. The CsI calorimeter energy scale is determined to better than 0.1% based on calibration using 500 million momentum analyzed electrons from $K_L \to \pi^\pm e^\mp \nu$ events. The momentum resolution of the spectrometer and the electromagnetic energy resolution of the CsI calorimeter are both better than 1%.

III. DATA COLLECTION

In this paper, we report results based on data taken during two periods in 1997, which will be referred to as "high intensity" and "low intensity." All five partial width ratios are measured in both the high and low intensity data samples. The quoted result for each ratio is based on the sample yielding the smaller total uncertainty; the other sample is used as a crosscheck. With the exception of $\Gamma_{K\mu3}/\Gamma_{Ke3}$, the high intensity sample gives a smaller uncertainty [41].

The high intensity period was used primarily to collect $K \to \pi\pi$ decays for the $Re(\epsilon'/\epsilon)$ measurement [1]. In addition to the nominal 2-pion triggers, several additional triggers with relaxed requirements were included for systematic studies; these additional triggers provide the data samples for the branching fraction analysis[42].

The low intensity data were collected during a 2-day

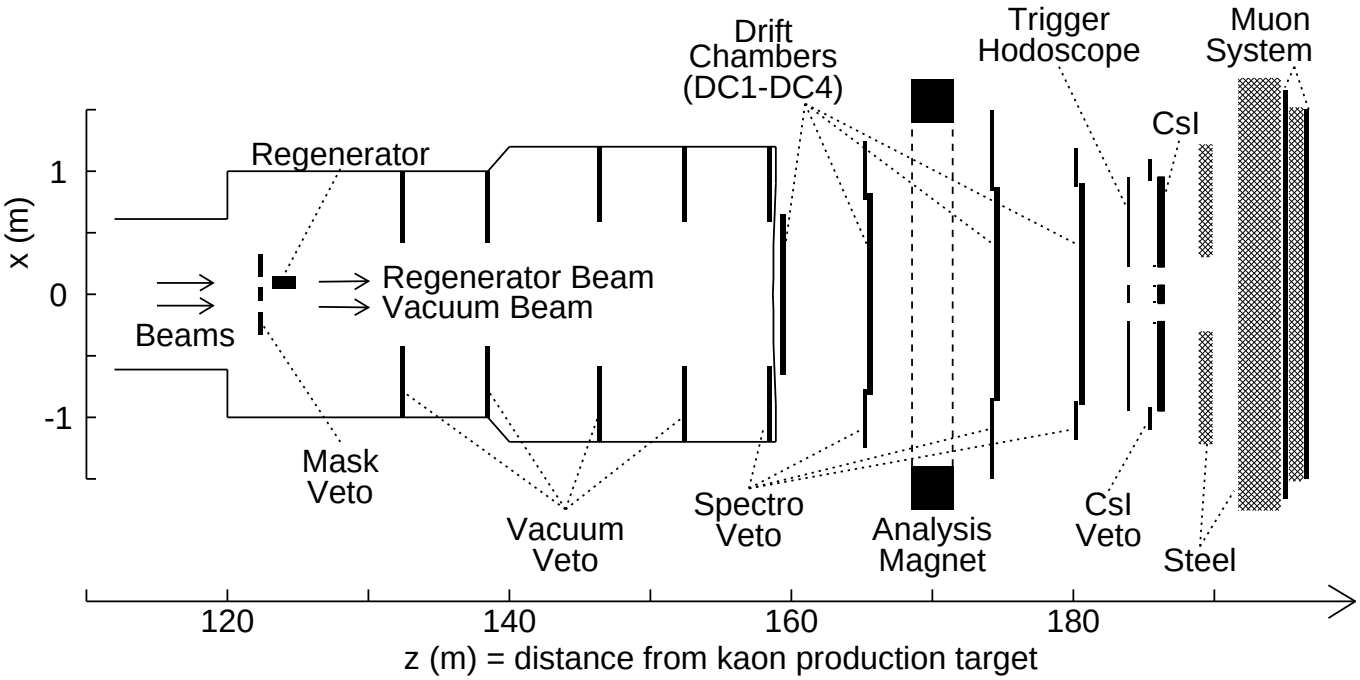

FIG. 1: Plan view of the KTeV (E832) detector. The evacuated decay volume ends with a thin vacuum window at $Z = 159$ m. The label "CsI" indicates the electromagnetic calorimeter.

special run. The beam intensity was lowered by a factor of 10, and the drift chamber operating voltage was raised to increase efficiency. In addition, the regenerator was removed, resulting in two vacuum beams and eliminating extra detector hits from the interaction of beam particles in the regenerator. The data collected during the low intensity period have significantly lower detector activity. For example, the average number of spurious drift chamber hits is only 2.3 in the low intensity period compared to 43 for the high intensity period.

IV. MEASUREMENT STRATEGY

The analysis is optimized to reduce systematic uncertainties resulting from the Monte Carlo simulation used to correct for acceptance differences between pairs of decay modes. With the exception of $\Gamma_{000}/\Gamma_{Ke3}$, we consider ratios of decay modes with similar final state particles. To be insensitive to the absolute trigger efficiency, events for the numerator and denominator of each partial width ratio are collected with a single trigger (the only exception is the measurement of Γ_{00}/Γ_{000} [43]).

The trigger requirements for each partial width ratio are summarized in Table I. The main trigger requirement for each pair of decay modes is either two charged tracks or a large energy deposit in the CsI calorimeter. For $\Gamma_{000}/\Gamma_{Ke3}$, the trigger requirement is only 25 GeV of energy in the calorimeter for both decay modes; there is no charged-track requirement for $K_L \to \pi^{\pm}e^{\mp}\nu$.

As will be described below, very simple event selection requirements may be used to distinguish different kaon decay modes from each other, and to reduce background to a negligible level for all decay modes. For some decay modes, the excellent spectrometer and calorimeter resolution allows us to achieve this background rejection without using all of the available detector information. For the $K_L \to \pi^{\pm}\mu^{\mp}\nu$ and $K_L \to \pi^{+}\pi^{-}\pi^{0}$ decay modes, we exploit this flexibility to reduce systematic uncertainties in the acceptance.

For the $K_L \to \pi^{\pm}\mu^{\mp}\nu$ decay mode, we do not make use of the muon system to identify the muon; this avoids systematic errors in modeling muon propagation in the steel in front of the muon hodoscope as well as in modeling

TABLE I: Trigger requirements used to measure each partial width ratio. Note that two different triggers are used to measure Γ_{00}/Γ_{000}. "Two charged tracks" refers to hits in the drift chambers and trigger hodoscope, "total CsI energy" requires more than 25 GeV energy-sum in the 3100 channels, "CsI clusters" refers to the number of clusters above 1 GeV, and "vetos" are used to reject events.

partial width ratio	two charged tracks	total CsI energy	CsI clusters	Vac, Spec vetos	CsI veto	muon veto
$\Gamma_{K\mu3}/\Gamma_{Ke3}$	yes	no	–	yes	no	no
$\Gamma_{+-0}/\Gamma_{Ke3}$	yes	no	–	no	no	yes
Γ_{+-}/Γ_{Ke3}	yes	no	–	yes	yes	yes
$\Gamma_{000}/\Gamma_{Ke3}$	no	yes	–	yes	no	yes
Γ_{00} for Γ_{00}/Γ_{000}	no	yes	4	yes	yes	yes
Γ_{000} for Γ_{00}/Γ_{000}	no	yes	6	yes	yes	yes

gaps between the muon counters. For the $K_L \to \pi^+\pi^-\pi^0$ decay mode, $\pi^0 \to \gamma\gamma$ is not reconstructed in order to be insensitive to pion showers that bias the photon energy measurement in the CsI calorimeter. Also, by ignoring the π^0, the reconstruction of $K_L \to \pi^+\pi^-\pi^0$ and $K_L \to \pi^\pm e^\mp \nu$ decays are very similar, reducing the uncertainty on the acceptance ratio of these two modes. As a crosscheck (Section VIII B), the $K_L \to \pi^\pm\mu^\mp\nu$ and $K_L \to \pi^+\pi^-\pi^0$ modes are also analyzed using the muon system and fully reconstructing the π^0.

All reconstructed decay modes are required to have kaon energy, E_K, between 40 and 120 GeV, and decay position, Z_K, between 123 and 158 m from the target. For the reconstruction of semileptonic and $K_L \to \pi^+\pi^-\pi^0$ decays, there is a missing particle (ν or π^0); this leads to multiple kaon energy solutions. All energy solutions are required to be in the accepted range. These E_K and Z_K ranges are more restrictive than in the ϵ'/ϵ analysis in order to have a negligible contribution from $K_S \to \pi\pi$ decays.

In the following two sections, we discuss the techniques used to reconstruct "charged" decay modes with two oppositely-charged particles, and "neutral" decay modes with only photons in the final state. More details of the KTeV event reconstruction are given in [1].

V. CHARGED DECAY MODE ANALYSIS

A. Charged Decay Mode Reconstruction and Event Selection

The reconstruction of $K_L \to \pi^\pm e^\mp \nu$, $K_L \to \pi^\pm\mu^\mp\nu$, $K_L \to \pi^+\pi^-\pi^0$, and $K_L \to \pi^+\pi^-$ begins with the identification of two oppositely charged tracks coming from a single vertex. To pass the event selection, one of the two tracks must be within 7 cm of a CsI cluster; the second track is not required to have a cluster match. As will be discussed later, this relaxed track-cluster matching requirement reduces the inefficiency arising from hadronic interactions upstream of the calorimeter.

The transverse (X, Y) decay vertex is required to be within an 11×11 cm^2 square centered on the beam (`RING` < 121 cm^2 [44]). The beam profile is about 10×10 cm^2 at the CsI calorimeter. This cut removes most events in which the kaon has scattered in a collimator.

The fiducial region for the charged decay modes is defined by requiring that projections of tracks fall safely within the boundaries of the drift chambers, trigger hodoscope, and the CsI calorimeter. The tracks are also subject to a "cell separation" cut [1], which requires that the tracks never share the same drift chamber cell. This requirement introduces an effective inner aperture, rejecting pairs of tracks with a very small opening angle. At the CsI calorimeter, the tracks are required to have a large 40 cm separation to minimize the overlap of hadronic and electromagnetic showers.

The different charged decay modes are distinguished from each other on the basis of particle identification and kinematics. The calorimeter energy measurement (E), combined with the spectrometer momentum (p), is used to distinguish electrons and pions. Figures 2(a) and (b) show data and Monte Carlo (MC) E/p distributions for electrons and pions, respectively. Electron candidates are required to have E/p greater than 0.92; this cut retains 99.8% of the electrons and rejects 99.5% of the pions. Pions are required to have E/p less than 0.92.

In the $K_L \to \pi^\pm\mu^\mp\nu$ analysis, the E/p requirement is used to reject K_{e3} decays. We also require that at least one track point to a CsI cluster with energy less than 2 GeV (Fig. 2(c)). The 2 GeV cluster requirement retains 99.7% of the $K_{\mu3}$ signal. This requirement does not distinguish the pion from the muon in 1/3 of the events, because 1/3 of the pions do not shower in the CsI calorimeter. Since the pion and muon are not identified, there are four E_K solutions that are all required to be within the 40-120 GeV range. Recall that muons are not identified with the muon system in order to reduce acceptance uncertainties; for the other decay mode analyses, however, the muon system is used in veto to suppress background from $K_{\mu3}$ and pion decays.

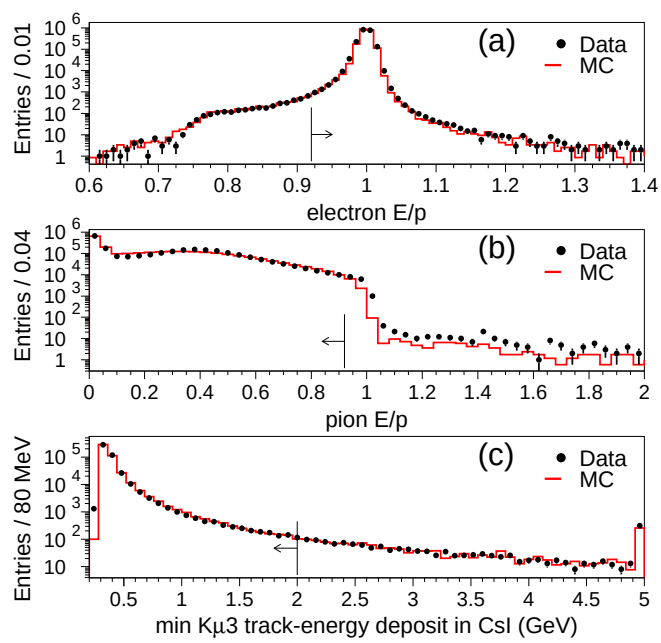

FIG. 2: (a) E/p (calorimeter energy over spectrometer momentum) distribution for electrons; (b) E/p distribution for pions; (c) minimum cluster energy deposit among two tracks for $K_{\mu3}$ decays (events with energy deposits greater than 5 GeV are shown in the last bin). The arrows indicate selection requirements.

In addition to particle identification for the two tracks, kinematic requirements are also used to distinguish the charged decay modes. We use three variables ($m_{\pi\pi}$, p_t^2, and k_{+-0}), each computed under the assumption that both tracks are charged pions. The only fully re-

constructed decay, $K_L \to \pi^+\pi^-$, is isolated using the two-track invariant mass ($m_{\pi\pi}$) and using the two-track transverse momentum-squared (p_t^2) measured with respect to the line connecting the primary target and decay vertex. To separate $K_L \to \pi^+\pi^-\pi^0$ from semileptonic decays, we use an additional kinematic variable,

$$k_{+-0} = \frac{\left(m_K^2 - m_{\pi\pi}^2 - m_{\pi^0}^2\right)^2 - 4m_{\pi\pi}^2 m_{\pi^0}^2 - 4m_K^2 p_t^2}{4(m_{\pi\pi}^2 + p_t^2)}, \tag{7}$$

where m_K and m_{π^0} are the kaon and π^0 masses, respectively. For $K_L \to \pi^+\pi^-\pi^0$ decays, k_{+-0} corresponds to the square of the longitudinal momentum of the π^0 in the reference frame in which the sum of the charged pion momenta is orthogonal to the kaon momentum.

To illustrate the use of these 3 variables, Fig. 3 shows data and MC distributions of $m_{\pi\pi}$, p_t^2, and k_{+-0} for all two-track events before particle identification and kinematic requirements are applied. The different MC samples are normalized to each other using the branching fractions reported in this paper. Figures 3(a) and (b) show peaked distributions in $m_{\pi\pi}$ and p_t^2 for $K_L \to \pi^+\pi^-$ decays. $K_L \to \pi^+\pi^-$ candidates are selected with $0.488 < m_{\pi\pi} < 0.508$ GeV/c^2 and $p_t^2 < 2.5 \times 10^{-4}$ GeV$^2/c^2$; the combined efficiency of these two requirements is 99.2%. For the other charged decay modes, the same $m_{\pi\pi}$ requirement is used to veto background from $K_L \to \pi^+\pi^-$ decays.

Figure 3(c) shows the k_{+-0} distribution. There are two well-separated enhancements, corresponding to semileptonic and $K_L \to \pi^+\pi^-\pi^0$ decays. We require $K_L \to \pi^+\pi^-\pi^0$ candidates to have $k_{+-0} > -0.005$ GeV$^2/c^2$, which retains 99.9% of the $K_L \to \pi^+\pi^-\pi^0$ decays. For semileptonic decays, we require $k_{+-0} < -0.006$ GeV$^2/c^2$; this keeps 99.5% of K_{e3} decays and 97.9% of $K_{\mu3}$ decays.

In addition to misidentifying kaon decay modes, background can also arise from hyperon decays. Background from $\Lambda \to p\pi^-$ decays is suppressed to a negligible level for all charged decay modes by removing events with invariant $p\pi^-$ mass consistent with m_Λ ($1.112 - 1.120$ GeV/c^2); to determine $m_{p\pi}$, the higher momentum track is assumed to be the proton.

Figures 4-6 show the data and MC distribution of $m_{\pi\pi}$, p_t^2, and k_{+-0} for each charged decay mode, after applying all event selection requirements except for the requirement on the plotted variable. The data and MC distributions agree well; the background for each signal mode is based on simulating the other three charged decay modes.

In addition to the general reconstruction and event selection described above, several notable features specific to certain decay modes are described below.

The $K_L \to \pi^\pm e^\mp \nu$ decay mode is used in four of the five partial width ratios. Some $K_L \to \pi^\pm e^\mp \nu$ selection requirements are adjusted depending on the ratio. For $\Gamma_{K\mu3}/\Gamma_{Ke3}$, the pion is required to satisfy a stricter E/p requirement ($E/p < 0.85$ instead of 0.92) to reduce background from K_{e3} in the $K_{\mu3}$ sample. This stricter E/p requirement retains 99.1% of pions, and rejects 99.93% of the electrons. Since there is one pion in the final state for both $K_{\mu3}$ and K_{e3}, we use the same strict E/p requirement in both decay modes to eliminate the systematic uncertainty from this requirement.

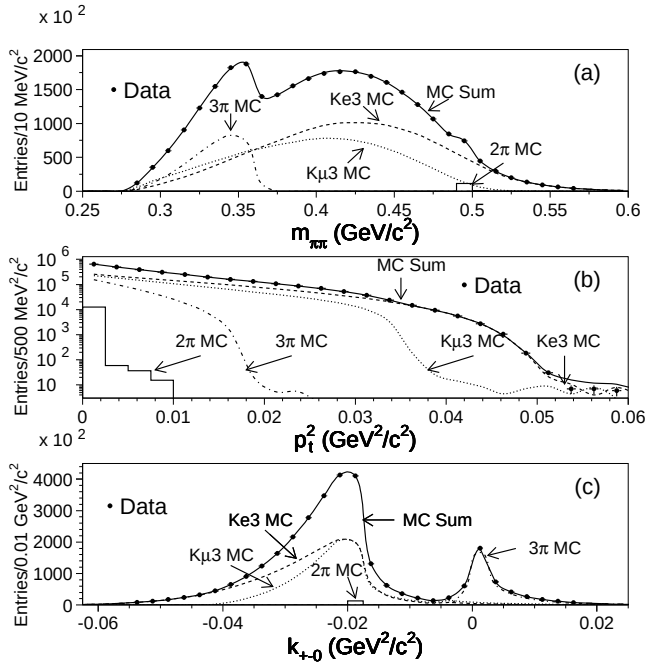

FIG. 3: For all two-track events, without particle identification or kinematic requirements, distributions are shown for (a) $m_{\pi\pi}$, (b) p_t^2, and (c) k_{+-0}. Data are shown as dots. MC simulations for $K_L \to \pi^\pm e^\mp \nu$, $K_L \to \pi^\pm \mu^\mp \nu$, $K_L \to \pi^+\pi^-\pi^0$, and $K_L \to \pi^+\pi^-$ are indicated. The sum of all MC contributions is shown as a solid line.

The measurement of $\Gamma_{000}/\Gamma_{Ke3}$ is based on a trigger that requires 25 GeV energy deposit in the CsI calorimeter. As discussed in Section IV, the minimum E_K requirement is 40 GeV, which is well above the 25 GeV trigger threshold. The E_K requirement ensures that the $K_L \to \pi^0\pi^0\pi^0$ acceptance is insensitive to the trigger threshold, but is not sufficient for K_{e3} decays because of the missing neutrino. For the K_{e3} acceptance to be insensitive to the trigger threshold, we require that the electron momentum be above 34 GeV/c.

Although the $K_L \to \pi^+\pi^-\pi^0$ decay mode is selected without reconstructing the π^0 in the CsI calorimeter, the π^0 decay products can hit the veto detectors. To eliminate the uncertainty in modeling the veto system efficiency, $\Gamma_{+-0}/\Gamma_{Ke3}$ is measured using a trigger that does not include the veto system. Photon clusters from the π^0 decay may also overlap a pion cluster resulting in an E/p measurement that is too high. To reduce the influence of this effect, pion candidates are allowed to have either E/p less than 0.92 or E/p greater than 1.05. Allowing pions with $E/p > 1.05$ recovers 1.5% of the $K_L \to \pi^+\pi^-\pi^0$ sample.

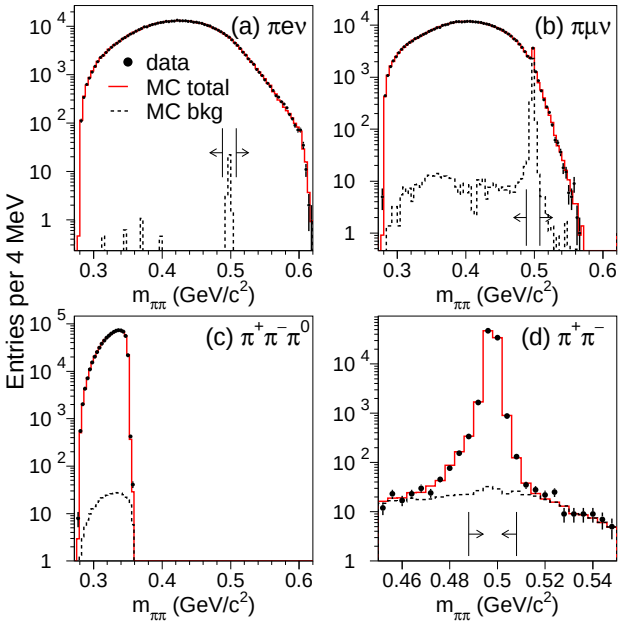

FIG. 4: $m_{\pi\pi}$ distributions after all analysis requirements except $m_{\pi\pi}$. Selection requirements are for (a) $K_L \to \pi^{\pm}e^{\mp}\nu$, (b) $K_L \to \pi^{\pm}\mu^{\mp}\nu$ (c) $K_L \to \pi^+\pi^-\pi^0$, (d) $K_L \to \pi^+\pi^-$. Data (MC) are shown by dots (histogram). "MC total" refers to signal plus background. "MC bkg" is the scattering+background prediction based on simulating the other three (non-signal) charged decay modes. The horizontal arrows indicate the region(s) selected by the $m_{\pi\pi}$ requirement. Note that the $m_{\pi\pi}$ scale is different in (d).

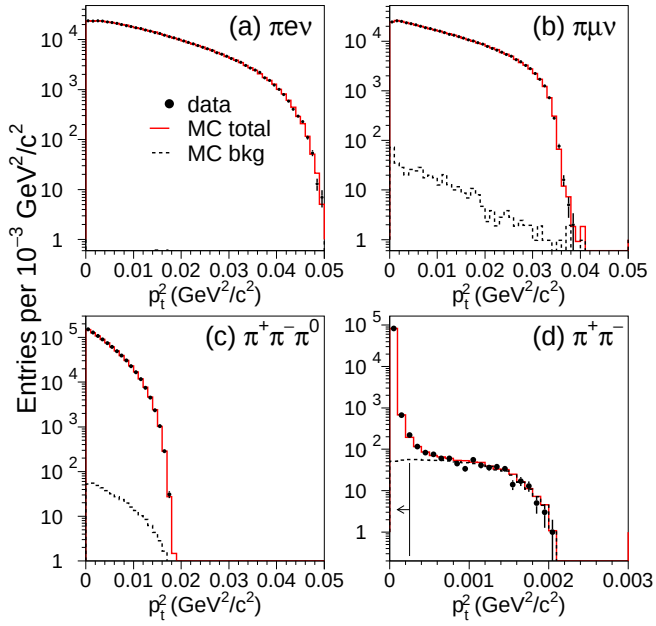

FIG. 5: p_t^2 distributions after all analysis requirements except p_t^2. Selection requirements are for (a) $K_L \to \pi^{\pm}e^{\mp}\nu$, (b) $K_L \to \pi^{\pm}\mu^{\mp}\nu$ (c) $K_L \to \pi^+\pi^-\pi^0$, (d) $K_L \to \pi^+\pi^-$. Data (MC) are shown by dots (histogram). "MC total" refers to signal plus background. "MC bkg" is the scattering+background prediction based on simulating the other three (non-signal) charged decay modes. The horizontal arrows indicate the region selected by the p_t^2 requirement. Note that the p_t^2 scale is different in (d).

B. Charged Decay Mode Background

Table II summarizes the background sources that are subtracted from each charged decay mode. The background to K_{e3} decays depends on the specific selection for the partial width ratio, but is always less than 3×10^{-5}. The background in the other three charged decays is $\sim 10^{-3}$. For the partially reconstructed decay modes ($K_L \to \pi^{\pm}e^{\mp}\nu$, $K_L \to \pi^{\pm}\mu^{\mp}\nu$, and $K_L \to \pi^+\pi^-\pi^0$), the background level is checked using the k_{+-0} distributions (Figure 6); based on the agreement of the data and Monte Carlo distributions, we assign a 20% systematic uncertainty to the background levels. The $K_L \to \pi^+\pi^-$ background is evaluated in the same manner as in the ϵ'/ϵ analysis [45].

There are also events in which the parent kaon has scattered in the defining collimator. This "collimator scattering" contribution includes a regenerated K_S-component, and therefore must be subtracted in the $K_L \to \pi^+\pi^-$ analysis; collimator scattering is suppressed to 0.01% using the p_t^2 requirement. For the partially reconstructed decay modes, collimator scattering is suppressed to 0.1% using the `RING` requirement; this scattering component is not subtracted, and is included in the samples for both data and MC.

TABLE II: Charged decay backgrounds from other kaon decays.

Decay Mode	Background ($\times 10^4$) to: K_{e3}	$K_{\mu 3}$	K_{+-0}	K_{+-}
K_{e3}	—	3	2.4	10
$K_{\mu 3}$	0.02	—	2.7	5
K_{+-0}	< 0.1	5	—	—
K_{+-}	< 0.2	3	—	1^a
Total	< 0.3	11	5	16

[a]This background is from collimator scattering.

VI. NEUTRAL DECAY MODE ANALYSIS

A. Neutral Decay Mode Reconstruction and Event Selection

The reconstruction of the $K_L \to \pi^0\pi^0$ and $K_L \to \pi^0\pi^0\pi^0$ decay modes is based on energies and positions of photons measured in the CsI electromagnetic calorimeter as described in [1]. Exactly four (six) clusters, each with a transverse profile consistent with a photon, are required for $K_L \to \pi^0\pi^0$ ($K_L \to \pi^0\pi^0\pi^0$). The clusters must be separated from each other by at least 7.5 cm and have energy greater than 3 GeV. The

fiducial volume is defined by cluster positions measured in the calorimeter. We reject events in which any cluster position is reconstructed in the layer of crystals adjacent to the beam holes (Fig. 12(a)) or in the outermost layer of crystals.

The center-of-energy of photon clusters is required to lie within an 11×11 cm^2 square centered on the beam profile (RING < 121 cm^2); the RING distribution for each neutral decay mode is shown in Fig. 7. The RING cut removes most events in which the kaon has scattered in the collimator or regenerator.

Photons are paired to reconstruct two or three neutral pions consistent with a single decay vertex. The number of possible photon pairings is 3 for $K_L \to \pi^0\pi^0$ and 15 for $K_L \to \pi^0\pi^0\pi^0$. To select the best pairing, we introduce a "pairing-χ^2" variable ($\chi^2_{\pi^0}$), which quantifies the consistency of the π^0 vertices. The pairing χ^2 is required to be less than 50 for $K_L \to \pi^0\pi^0$ and less than 75 for $K_L \to \pi^0\pi^0\pi^0$ [46]. This procedure identifies the correct photon pairing in more than 99% of the events. The Z_K location of the kaon decay vertex is determined from a weighted average of the π^0 vertices. The main kinematic requirement is that the invariant mass of the $2\pi^0$ or $3\pi^0$ final state (Fig. 8) be between 0.490 and 0.505 GeV/c^2.

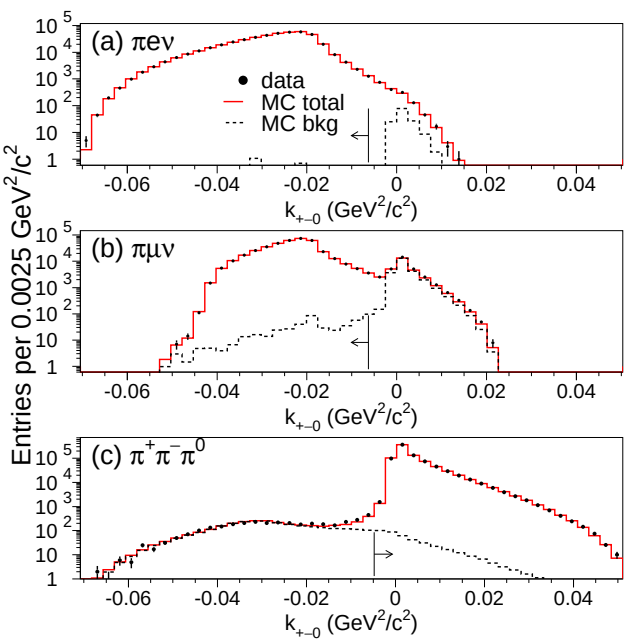

FIG. 6: k_{+-0} distributions after all analysis requirements except k_{+-0}. Selection requirements are for (a) $K_L \to \pi^\pm e^\mp \nu$, (b) $K_L \to \pi^\pm \mu^\mp \nu$, (c) $K_L \to \pi^+\pi^-\pi^0$. Data (MC) are shown by dots (histogram). "MC total" refers to signal plus background. "MC bkg" is the scattering+background prediction based on simulating the other three (non-signal) charged decay modes. The horizontal arrows indicate the region selected by the k_{+-0} requirement.

B. Neutral Decay Mode Backgrounds

The background subtraction procedure for $K_L \to \pi^0\pi^0$ is identical to that used in the ϵ'/ϵ analysis. The background composition is 0.30% from scattering in the regenerator, 0.09% from collimator scattering, and 0.32% from $K_L \to \pi^0\pi^0\pi^0$ in which two photons are undetected ("$3\pi^0$-background") [47]. The total background is (0.71 ± 0.06)%.

In Fig. 7(a), events with RING > 200 cm^2 are almost entirely due to scattering in the regenerator and collimator; the MC predicts both the absolute level and RING-shape. Note that events with scattered kaons have the same invariant-mass distribution as events with unscattered kaons, and therefore cannot be identified in the $\pi^0\pi^0$ mass distribution (Fig. 8(a)).

In Fig. 8(a), 97% of the events outside the signal region result from misreconstructed $K_L \to 3\pi^0$ events and the remaining 3% are from from $K_L \to \pi^0\pi^0$ events with the wrong photon pairing. These mass sidebands are well modeled in the simulation. The $3\pi^0$-background is responsible for the apparent increase in background under the RING-signal in Fig. 7(a).

In the $K_L \to \pi^0\pi^0\pi^0$ decay mode, no source of background has been identified. The contribution from kaon scattering (0.1% after the RING cut) is not subtracted; it is well modeled in the simulation, as shown in Fig. 7(b). The mass side-bands in Fig. 8(b) and (c) result from $K_L \to \pi^0\pi^0\pi^0$ decays in which the wrong photon pairing is used to compute the invariant mass. These mispairings, which are well modeled by the MC, are not subtracted.

VII. MONTE CARLO SIMULATION AND SYSTEMATIC UNCERTAINTIES

A detailed Monte Carlo simulation is used to determine the acceptance for each decay mode. These acceptances are used to correct the background-subtracted numbers of events for each partial width ratio. The acceptance, A_i for decay mode "i", is defined as

$$A_i \equiv N_i^{rec}/N_i^{gen}, \tag{8}$$

where N_i^{gen} is the number of events generated within the nominal E_K and Z_K ranges, and N_i^{rec} is the number of reconstructed events [48]. To account for radiative effects and resolution, which can cause reconstructed events to migrate across the E_K and Z_K boundaries, N_i^{rec} is determined from a Monte Carlo generated with broader E_K and Z_K ranges.

The systematic uncertainties for this analysis, which are summarized in Table III, fall into the following categories: acceptance, background, external branching ratios, and MC statistics. Uncertainties in acceptance, which result from imperfections in the Monte Carlo simulation, are by far the most important.

TABLE III: Systematic uncertainties in partial width ratios (in percent)

Source of uncertainty	$\Gamma_{K\mu3}/\Gamma_{Ke3}$	$\Gamma_{000}/\Gamma_{Ke3}$	$\Gamma_{+-0}/\Gamma_{Ke3}$	Γ_{+-}/Γ_{Ke3}	Γ_{00}/Γ_{000}
Acceptance (MC Simulation)					
Event Generation:					
- Kaon energy spectrum	0.02	0.16	0.04	0.02	0.01
- Form factor	0.11	0.08	0.29	0.08	0.00
Radiative corrections:					
-	0.15	0.20	0.14	0.14	0.00
Particle Propagation:					
- Detector material	0.10	0.56	0.33	0.33	0.15
- Detector geometry	0.02	0.39	0.05	0.02	0.08
Detector Response:					
- Accidental activity	0.00	0.22	0.04	0.02	0.03
- Trigger	0.00	0.07	0.10	0.07	0.28
- $e^{\pm}, \mu^{\pm}, \pi^{\pm}$ reconstruction	0.21	0.70	0.24	0.26	0.00
- π^0 reconstruction	0.00	0.37	0.00	0.00	0.23
Background	0.10	0.00	0.02	0.04	0.04
$B(\pi^0 \to \gamma\gamma)$	0.00	0.10	0.10	0.00	0.03
Monte Carlo Statistics	0.10	0.12	0.05	0.13	0.16
Total	0.33	1.12	0.55	0.47	0.44

The Monte Carlo simulation includes four main steps, each of which introduces systematic uncertainties in the acceptance: event generation, radiative corrections, propagation of particles through the detector, and detailed simulation of detector response. In the following sections, we will discuss these MC steps as well as the associated systematic uncertainties.

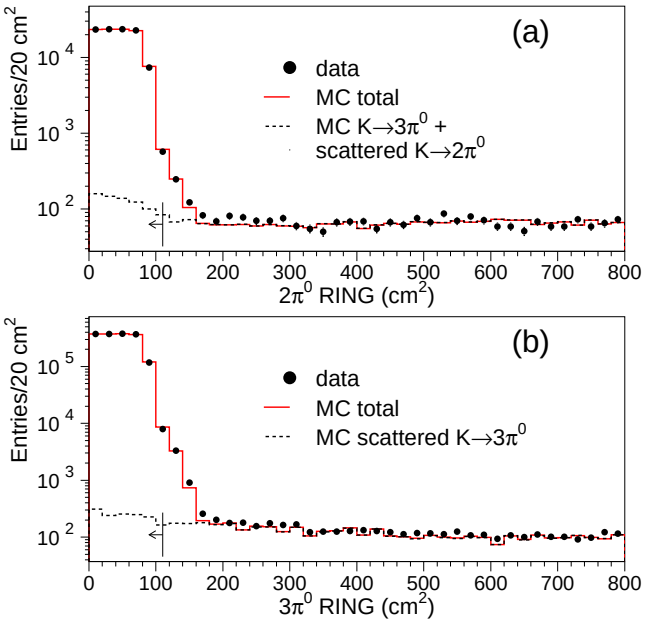

FIG. 7: `RING` distribution for (a) $K_L \to \pi^0\pi^0$ and (b) $K_L \to \pi^0\pi^0\pi^0$ candidates. Data are shown with dots. "MC total" (histogram) refers to the simulation of the signal including backgrounds and scattering in the collimator and regenerator. The dashed histogram shows scattering+background predicted by MC. The arrow indicates the analysis requirement.

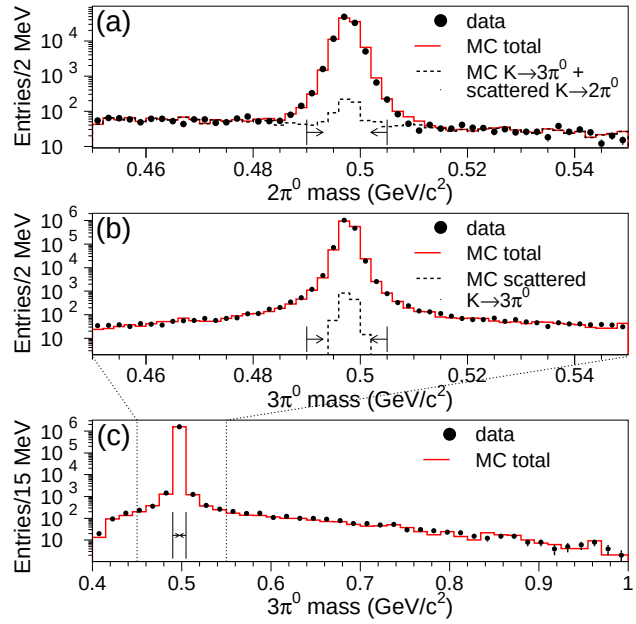

FIG. 8: (a) $2\pi^0$ mass, (b) $3\pi^0$ mass, and (c) $3\pi^0$ mass shown with extended mass scale. Data are shown with dots. "MC total" (histogram) refers to the simulation of the signal including backgrounds scattering in the collimator and regenerator. The dashed histogram shows scattering+background predicted by MC. The arrows indicate the analysis requirement.

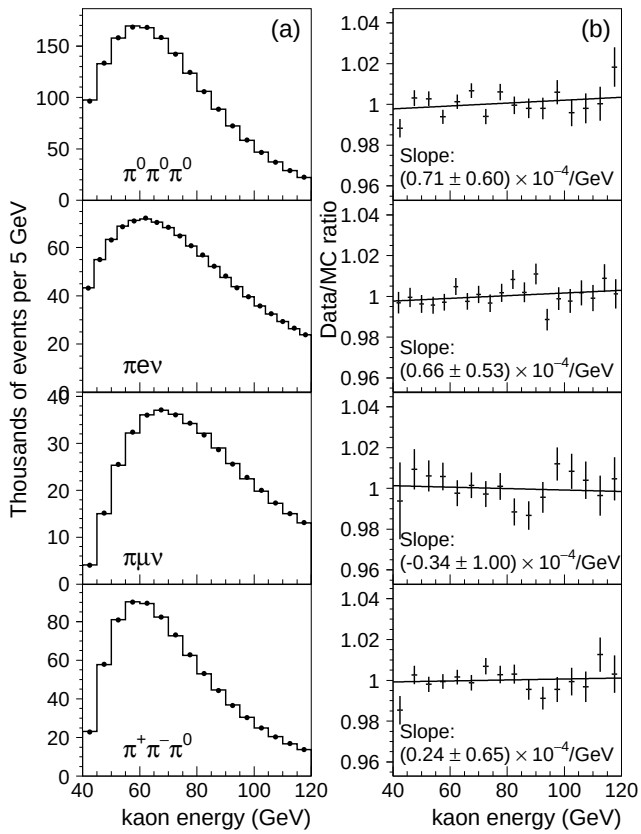

FIG. 9: Comparison of the vacuum beam kaon energy distributions for data (dots) and MC (histogram). For the semileptonic and K_{+-0} modes, the highest E_K solution is plotted. The data-to-MC ratios on the right are fit to a line, and the E_K-slopes are shown.

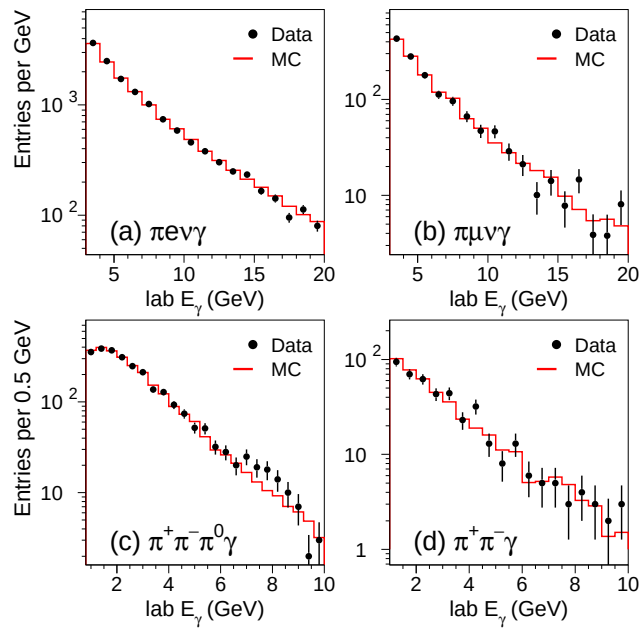

FIG. 10: Comparison of the energy distribution for radiative photon candidates for each of the charged decay modes. The data are shown as dots and the MC as a histogram.

A. Event Generation

Event generation starts by selecting a kaon energy from a spectrum tuned with 10 million $K_L \to \pi^+\pi^-$ events [1]. Figure 9 shows data-to-MC comparisons of the reconstructed energy for the four main K_L decay modes. To limit possible acceptance biases in the determination of this spectrum, we compare the high-statistics $K_L \to \pi^+\pi^-$and $K_L \to \pi^0\pi^0$ spectra from the ϵ'/ϵ samples. These spectra agree to better than 1% for kaon energies between 40 and 120 GeV (or 0.01% per GeV). For each partial width ratio, the systematic uncertainty is based on this 0.01%/GeV E_K-slope uncertainty and the difference between the average kaon energy of the two decay modes.

The decay kinematics for the 3-body decay modes depends on form factors. For the $K_L \to \pi^+\pi^-\pi^0$ and $K_L \to \pi^0\pi^0\pi^0$ decay modes, PDG [2] values of the form factors with 2 sigma uncertainties are used. For semileptonic form factors we use our own measurements [3]. The largest uncertainty from form factors is in the $K_L \to \pi^+\pi^-\pi^0$ decay mode.

B. Radiative Corrections

For K_{e3} and $K_{\mu3}$, inner bremsstrahlung (IB) contributions are accounted for using a new program, `KLOR`, described in [4]. `PHOTOS` [5] is used to generate the IB contribution in $K_L \to \pi^+\pi^-\pi^0$ decays. The simulation of the $K_L \to \pi^+\pi^-$ decay mode includes IB contributions, but does not include the direct emission component, which has a negligible impact on this analysis.

To check the simulation of IB, we have performed an analysis for each charged decay mode in which high-energy radiated photons are identified in the CsI calorimeter. Figure 10 shows the data and MC energy distribution for radiative photon candidates in the laboratory frame; the shape and normalization agree for all decay modes.

The simulation without IB changes the acceptance by 2-3% for the K_{e3} mode, depending on the electron energy requirement, and less than 0.5% for the other modes. The systematic uncertainty in the partial width ratios is taken to be 6% of the acceptance change from IB based on our study of radiative decays. The resulting uncertainties vary from 0.14% to 0.20%.

C. Particle propagation

Once a kaon decay is generated, the decay products and their secondaries are propagated through the detector. This propagation includes both electromagnetic and hadronic interactions of particles with detector material,

and requires precise modeling of the detector geometry and composition. To model interactions in the detector, GEANT [6] is used to generate process-specific libraries that are used by our MC.

1. Detector Material

a. Electromagnetic interactions in detector material include photon conversions, Bremsstrahlung, multiple scattering, and δ-ray production. For photon conversions and Bremsstrahlung, most particle losses in the reconstruction result from interactions upstream of the analysis magnet. For multiple scattering and δ-ray production, interactions up to the last drift chamber (DC4) are important. We estimate 0.73% radiation lengths of material upstream of the analysis magnet, and a total of 1.18% radiation lengths of material through DC4.

To check our estimate of detector material upstream of the analysis magnet, we study $K_L \to \pi^{\pm} e^{\mp} \nu$ decays in which an external Bremsstrahlung photon is identified in the CsI calorimeter. In this study, we take advantage of the magnet kick to separate the electron from the Bremsstrahlung photon. Figure 11(a) illustrates a K_{e3} decay in which a photon is produced in DC2. Figure 11(b) shows the distribution of distances ($\Delta R_{\gamma\mathrm{brem}}$) between the candidate photon cluster and the extrapolation of the electron trajectory (measured in DC1+DC2) to the CsI calorimeter. The peak in Fig. 11(b) is mainly from external Bremsstrahlung, while the high-side shoulder is from radiative $K_L \to \pi^{\pm} e^{\mp} \nu\gamma$ decays. To isolate events with external Bremsstrahlung, we require $\Delta R_{\gamma\mathrm{brem}} < 1$ cm; the background from radiative $K_L \to \pi^{\pm} e^{\mp} \nu\gamma$ events is 43%. The MC sample is normalized to the total number of K_{e3} decays in data; the fraction of events with a Bremsstrahlung photon in this study is the same in data and MC to within 5%.

The material downstream of the analysis magnet (including the 0.027 X_0 trigger hodoscope) is checked with $K_L \to \pi^0\pi^0\pi^0$ decays in which one or more of the photons converts and gives hits in the hodoscope [49]. The fraction of events with hodoscope hits is measured to be (13.06 ± 0.03)% in data and (12.91 ± 0.03)% in MC.

The simulation of δ-rays and multiple scattering each use a GEANT-based library. The δ-ray simulation is tuned to data using DC signals recorded at earlier times than expected based on the track location in the DC cell. To check the δ-ray simulation, we consider the case in which a δ-ray drifts from one drift chamber cell into a neighboring cell and leaves an extra hit adjacent to the track. This effect is observed in 35% of the events in data (corresponding to about 2% probability per wire-plane), and 30% of the MC events. We therefore assign a 15% uncertainty to the δ-ray simulation. The uncertainty in our simulation of multiple scattering is estimated to be 10% of its effect on the acceptance, based on data-MC comparisons of the matching of charged particle trajectories at the decay vertex.

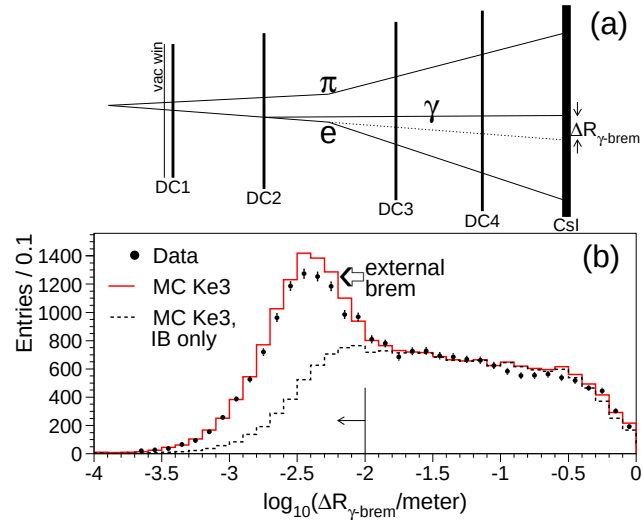

FIG. 11: (a) Illustration of electron Bremsstrahlung at DC2 for a $K_L \to \pi^{\pm} e^{\mp} \nu$ decay. The dotted line is extrapolated from the upstream electron trajectory to the CsI. The track bend between DC2 and DC3 is from the magnet kick. (b) Measured distribution of $\Delta R_{\gamma\mathrm{brem}}$. Data are shown by dots, and MC K_{e3} by histogram. The MC contribution from radiative $K_L \to \pi^{\pm} e^{\mp} \nu\gamma$ is shown by the dashed histogram. The MC sample is normalized to the total number of K_{e3} candidates in data.

b. Hadronic interactions of charged pions can result in broad showers that lead to tracking losses and energy deposits in veto detectors. Pion interactions in the spectrometer and trigger hodoscope are simulated with GEANT-based libraries. Interactions in material up through the last drift chamber (0.7% pion interaction lengths) usually result in track loss. We assign a 50% uncertainty on this source of track loss, as described in Appendix A. The corresponding 0.35% uncertainty in pion track-loss affects partial width ratios with a different number of charged pions in the numerator and denominator.

Pion interactions in the trigger hodoscope (1.2% pion interaction lengths) downstream of the charged spectrometer often prevent the track from matching a cluster in the CsI calorimeter. These interactions also can produce hadronic showers that deposit energy in the CsI-Veto. The inefficiency of the track-cluster match requirement for pions is 0.6% for data and 0.5% for MC. The associated systematic uncertainties in the partial width ratios are negligible because only one of the two tracks is required to match a cluster. The CsI-Veto is only used in the trigger for Γ_{+-}/Γ_{Ke3} (Table I); the loss is measured to be (0.4 ± 0.2)% and is included in the MC.

Most charged pions that do not decay interact hadronically in the CsI or muon system steel. The fraction of pions that penetrate the steel and produce a signal in the muon hodoscope is measured with fully reconstructed $K_L \to \pi^+\pi^-\pi^0$ decays from the low intensity sample; the fraction is determined to be $(1.0 \pm 0.1) \times 10^{-4} p_{\pi}$, where

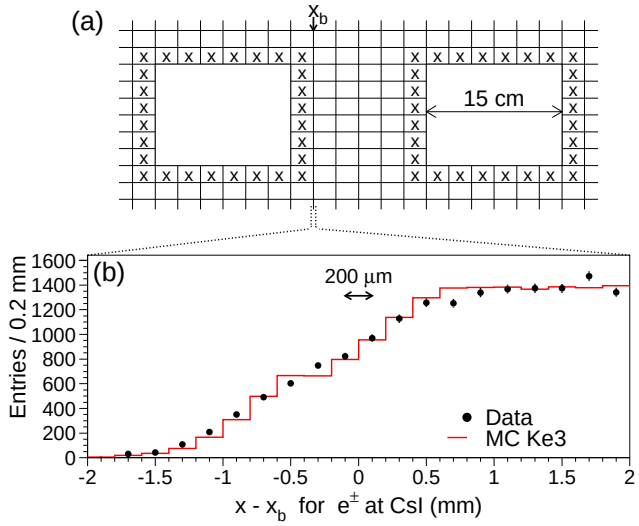

FIG. 12: (a) layout of inner CsI region near beam-holes. Photons with reconstructed CsI position in a crystal adjacent to a beam hole (marked with an "X") are rejected in the analysis. x_b is the coordinate at one of the crystal boundaries that defines the photon acceptance. (b) For $K_L \to \pi^{\pm}e^{\mp}\nu$ decays, $x - x_b$ for electrons at the CsI determined by extrapolating the trajectory measured in the spectrometer. The CsI position requirement in (a) is applied to this electron sample. The 200 μm wide arrow indicates the systematic uncertainty for this photon aperture.

p_π is the pion momentum in GeV/c.

2. *Detector Geometry*

The dimensions of the four drift chambers are known to better than 20μm based on optical surveys. The spectrometer is aligned in situ as explained in [1]. The CsI inner aperture for photons is illustrated in Fig. 12(a). This aperture is measured by comparing extrapolated electron tracks measured in the spectrometer with cluster positions measured in the calorimeter (Fig. 12(b)); the uncertainty in this aperture size is 200μm. The calorimeter dimensions (1.9 m $\times$ 1.9 m) are known to better than 1mm.

The agreement of data and MC decay vertex distributions (Fig. 13) provides a sensitive overall check of the detector geometry. For each partial width ratio, the systematic uncertainty is the product of the data/MC Z_K-slope and the difference between the average reconstructed Z_K of the two decay modes.

D. Detector Response

The Monte Carlo includes a detailed simulation of detector response to different particle species, as well as the effect of accidental activity.

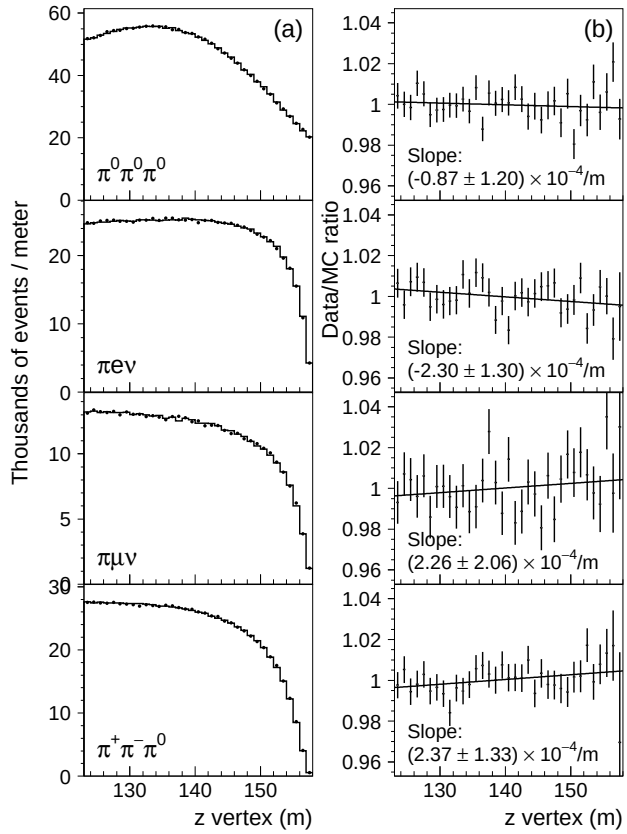

FIG. 13: Comparison of the vacuum beam z distributions for data (dots) and MC (histogram). The data-to-MC ratios on the right are fit to a line, and the z-slopes are shown.

1. *Accidentals*

Accidental detector activity is measured with a trigger that is proportional to the instantaneous beam intensity. We overlay an accidental data event on each generated decay in the Monte Carlo simulation. Based on data-MC comparisons of extra detector activity, the systematic uncertainty is estimated to be 10% of the acceptance change arising from overlaying accidental data events in the simulation. The effects of accidentals result in 0.22% uncertainty in the $\Gamma_{000}/\Gamma_{Ke3}$ ratio, and less than 0.04% in the other partial width ratios.

2. *Trigger*

As described in [1], the KTeV MC includes a detailed trigger simulation. Although the analysis requirements are designed to be stricter than the trigger, potential anomalies in the trigger pre-scales and signal processing could result in losses that are not simulated. The general strategy to estimate these effects is to use K_{e3} decays from a charged-track trigger to study the total CsI energy trigger (Table I), and to use charged decay

modes collected in the total-energy trigger to study the charged-track trigger.

For partial width ratios in which events for the numerator and denominator are collected with the same trigger, uncertainties in trigger efficiency largely cancel, and resulting uncertainties are less than 0.1%. For Γ_{00}/Γ_{000}, the only ratio measured with two separate triggers, the systematic uncertainty from the trigger efficiency is 0.28%.

3. Response to Charged Particles

Each charged decay mode includes a different combination of $e^{\pm}$, $\pi^{\pm}$, and $\mu^{\pm}$. The simulation of the drift chamber response includes measured wire inefficiencies, and several subtle effects that cause non-Gaussian tails in the position resolution [1]. To simulate the response in the CsI calorimeter, a separate GEANT library is generated for $e^{\pm}$, $\pi^{\pm}$, and $\mu^{\pm}$. Tails in the CsI energy response are measured in data as described in Appendix B.

Sources of systematic uncertainty are the tracking efficiency, drift chamber calibration, tails in the E/p distribution, and analysis cut variations. The uncertainty in the drift chamber efficiency is 0.6% as explained in Appendix A; this uncertainty affects only the $\Gamma_{000}/\Gamma_{Ke3}$ ratio. The DC calibration introduces a systematic uncertainty less than 0.1% on each ratio. The effect of tails in the CsI energy response introduces systematic uncertainties well below 0.1% on the charged partial width ratios. Cut variation studies introduce a 0.2% uncertainty on all partial width ratios.

4. Response to Photons

The CsI calorimeter response to photons is simulated with a GEANT library. The low-side tail in the energy response is assumed to be the same as for electrons (Appendix B). The most crucial role of the photon simulation is to predict the efficiency of reconstructing the $K_L \to \pi^0\pi^0\pi^0$ decay mode for the $\Gamma_{000}/\Gamma_{Ke3}$ ratio. The sources of systematic uncertainty in reconstruction of multi-π^0 events are: photon pairing efficiency, energy scale, and photon reconstruction efficiency.

The pairing efficiency study uses $K_L \to \pi^0\pi^0\pi^0$ decays since there is no background after identifying six photon clusters in the CsI calorimeter. The sidebands in the $3\pi^0$ invariant mass distribution, as well as events with $\chi^2_{\pi^0}$ values beyond the selection cut, result from misreconstructed $K_L \to \pi^0\pi^0\pi^0$ events. These misreconstructed events result almost entirely from selecting the incorrect photon pairing. Fig. 8(c) illustrates misreconstructed events in the $3\pi^0$ invariant mass distribution. The MC sample in Fig. 8(c) is normalized to data in the 15 MeV wide signal region; the data and MC sidebands are in good agreement. The combined requirements on $\chi^2_{\pi^0}$ and $3\pi^0$ invariant mass remove $(0.80 \pm 0.01)\%$ of the $K_L \to \pi^0\pi^0\pi^0$ events in data, and remove $(0.66 \pm 0.01)\%$ of the events in MC. This 0.14% difference is included as a systematic uncertainty on the $\Gamma_{000}/\Gamma_{Ke3}$ ratio.

Uncertainties in the calorimeter energy scale and linearity affect the π^0 reconstruction efficiency, primarily because of the photon energy and kaon energy requirements. The systematic uncertainty is based on the same set of tests as in the ϵ'/ϵ analysis; these tests result in a 0.33% uncertainty on the $\Gamma_{000}/\Gamma_{Ke3}$ ratio, and a 0.05% uncertainty on the Γ_{00}/Γ_{000} ratio.

We consider three sources of uncertainty in the photon reconstruction efficiency: detector readout, dead material, and CsI cluster shape requirements. The calorimeter readout inefficiency is monitored with a laser system, and is measured to be less than 10^{-6}. The amount of dead material between crystals is checked with muons, and is included in the MC; the probability of losing a photon because of this dead material is less than 10^{-5}. The effect of the photon cluster shape requirement for γ candidates in the calorimeter is studied by removing this cut in the $\Gamma_{000}/\Gamma_{Ke3}$ analysis; the corresponding change of 0.05% is taken as a systematic uncertainty.

E. Sensitivity to π^0 Branching Fractions

For decay modes that use $\pi^0 \to \gamma\gamma$ decays, we correct for the branching ratio, $B(\pi^0 \to \gamma\gamma) = 0.9880 \pm 0.0003$. The decay $\pi^0 \to e^+e^-\gamma$ has a negligible effect on all decay mode acceptances except for $K_L \to \pi^+\pi^-\pi^0$. Although the measurement of $K_L \to \pi^+\pi^-\pi^0$ ignores the π^0, it is still sensitive to the $\pi^0 \to e^+e^-\gamma$ decay because the extra tracks can cause the event to be rejected. This effect is studied using a MC sample of $K_L \to \pi^+\pi^-\pi^0$ decays in which the π^0 decays to $e^+e^-\gamma$; the acceptance for this MC sample is $0.32 \times A_{+-0}$, where A_{+-0} is the nominal acceptance for $K_L \to \pi^+\pi^-\pi^0$ with $\pi^0 \to \gamma\gamma$. We assign a 20% uncertainty to the fraction of these events passing the selection, resulting in a 0.1% uncertainty in the $\Gamma_{+-0}/\Gamma_{Ke3}$ partial width ratio.

VIII. RESULTS

A. Partial width ratios

The numbers of events and detector acceptances for all decay modes are summarized in Table IV; the resulting partial width ratios are given in the last column of the table. For each partial width ratio, the first error is statistical and the second systematic. The systematic uncertainty is calculated as the sum in quadrature of the individual sources. Note that although the partial width ratios use independent data samples, there are correlations among the systematic errors. For example, uncertainties from external bremsstrahlung cause correlated uncertainties among the four partial width ratios involving Γ_{Ke3}. These correlations are treated as described in

Appendix D of Ref. [1]. The correlation coefficients for the five partial width ratios are given in Table V.

The systematic precision of each ratio depends on the cancellation of systematic uncertainties for the pair of modes. Among the partial width ratios, the measurement of $\Gamma_{000}/\Gamma_{Ke3}$ has the largest systematic uncertainty, with $\sigma_{syst} = 1.12\%$. This ratio has the largest uncertainty because there is no cancellation of the 0.6% uncertainty in the tracking efficiency, as well as the 0.37% uncertainty in the $3\pi^0$ reconstruction. Pairs of modes with the same number of charged pions in the final state ($\Gamma_{K\mu3}/\Gamma_{Ke3}$ and Γ_{00}/Γ_{000}) have the smallest systematic uncertainty, with $\sigma_{syst} \sim 0.4\%$. Pairs of modes in which the number of charged pions is different ($\Gamma_{+-0}/\Gamma_{Ke3}$ and Γ_{+-}/Γ_{Ke3}) have a larger systematic uncertainty of $\sigma_{syst} \sim 0.55\%$; this increased uncertainty is mainly from the 0.35% uncertainty in losses from hadronic interactions.

B. Cross Checks of Partial Width Ratios

We have performed several crosschecks of our measurements. Some of these checks affect all of the partial width ratios, while others are relevant to a specific decay mode.

As discussed in Sec. III, we measure each partial width ratio in both high and low intensity data samples. The factor of 10 difference in beam intensity between these samples results in significantly different tracking and photon cluster reconstruction efficiencies. For example, the tracking inefficiency is nine times smaller in the low intensity sample (0.38% vs. 3.3%). Figure 14 compares the partial width ratios measured in these two samples. The measurements are in good agreement: the χ^2 per degree of freedom is 3.4/5.

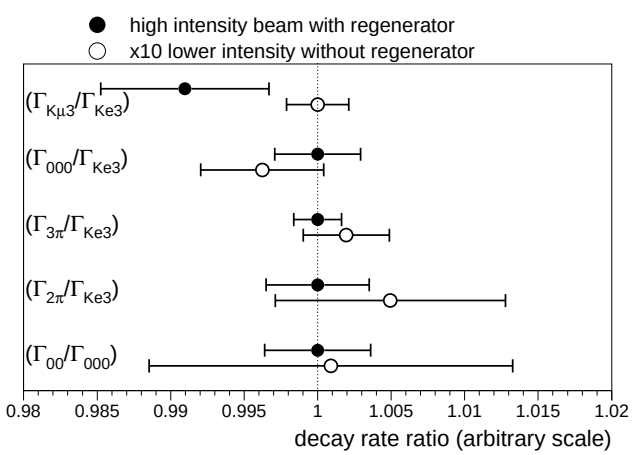

FIG. 14: Partial width ratios measured with high intensity (solid dots) and with low intensity (open circles). Each ratio is normalized so that the quoted result is one. The error bars reflect the statistical uncertainties between the two samples.

To check our nominal $K_L \to \pi^\pm\mu^\mp\nu$ analysis, which does not use the muon system, we perform an analysis that requires one track to be matched to hits in the most downstream muon hodoscope. Since the muon track is identified, there are only 2 kaon energy solutions instead of the 4 solutions in the nominal analysis. This alternate analysis differs from the nominal analysis by $(0.08 \pm 0.02_{\rm stat})\%$. It is worth mentioning that requiring a signal in the muon hodoscope does not significantly reduce the background because $K_L \to \pi^+\pi^-\pi^0$ and $K_L \to \pi^+\pi^-$ decays can pass the $K_{\mu3}$ selection only if one of the pions decays in flight.

The nominal $K_L \to \pi^+\pi^-\pi^0$ analysis, which does not reconstruct the π^0, is checked by performing an analysis in which the $K_L \to \pi^+\pi^-\pi^0$ decay is fully reconstructed using the $\pi^0 \to \gamma\gamma$ decay. Requiring a reconstructed $\pi^0 \to \gamma\gamma$ decay in the CsI calorimeter reduces the acceptance by a factor of four. To increase the statistical significance of this crosscheck, we use an independent sample (with $\times 5$ smaller pre-scale) collected in the trigger used to measure Γ_{+-}/Γ_{Ke3} (see Table I); the two methods agree to $(0.03 \pm 0.28_{\rm stat})\%$.

The stability of the results is also tested by dividing the data into a variety of subsamples based on criteria such as vertex position, kaon energy, minimum track separation, and minimum photon energy. The measured partial width ratios are found to be consistent within the uncorrelated statistical uncertainty in all of these studies.

The clean separation of semileptonic and $K_L \to \pi^+\pi^-\pi^0$ decays in the k_{+-0} distribution (Fig. 3(c)) allows a measurement of $R_{+-0} = \Gamma_{+-0}/(\Gamma_{K\mu3} + \Gamma_{Ke3} + \Gamma_{+-0})$ that does not use any particle identification information. The difference between this fit and the nominal analysis is $(0.35 \pm 0.51)\%$.

Assuming lepton universality, we can make an independent prediction of the $\Gamma_{K\mu3}/\Gamma_{Ke3}$ ratio:

$$\left[\frac{\Gamma_{K\mu3}}{\Gamma_{Ke3}}\right]_{pred} = \frac{1+\delta_K^\mu}{1+\delta_K^e} \cdot \frac{I_K^\mu}{I_K^e}. \tag{9}$$

Here, δ_K^ℓ represents the mode-dependent long-distance radiative correction to the total decay width, and I_K^e and I_K^μ are the decay phase space integrals, which depend on the form factors. Using the KTeV measurement of $I_K^\mu/I_K^e = 0.6622 \pm 0.0018$ [3] and $(1+\delta_K^\mu)/(1+\delta_K^e) = 1.0058 \pm 0.0010$ from KLOR [4], we find that the ratio of the directly measured to predicted values of $\Gamma_{K\mu3}/\Gamma_{Ke3}$ is 0.9969 ± 0.0048, consistent with 1.

C. Determination of Branching Fractions, Partial Decay Widths, and $|\eta_{+-}|$

Imposing the constraint that the sum of the six largest branching fractions is 0.9993, we determine the branching fractions shown in Table VI. Correlations among the partial decay width measurements (Table V) are taken into account in calculating uncertainties in the branching fractions. The correlation coefficients for the six branching fractions are given in Table VII. Using the PDG average for the neutral kaon lifetime [50],

TABLE IV: Background-subtracted numbers of events, detector acceptances, and resulting ratios of partial decay widths. The $\times x$ next to a number of events reflects a prescale that must be applied to calculate the partial width ratio. For the partial width ratios, the first error is statistical and the second systematic. Note that differences in event selection requirements for the partial width ratios result in a range of acceptances for $K_L \to \pi^{\pm}e^{\mp}\nu$.

Decay Modes	Numbers of Events	Acceptance	Partial Width Ratio
$\Gamma_{K\mu3}/\Gamma_{Ke3}$	394300/449379	0.239/ 0.180	$0.6640 \pm 0.0014 \pm 0.0022$
$\Gamma_{000}/\Gamma_{Ke3}$	209365/211950	0.046/ 0.022	$0.4782 \pm 0.0014 \pm 0.0053$
$\Gamma_{+-0}/\Gamma_{Ke3}$	799501/(807343 $\times$ 2)	0.200/ 0.124	$0.3078 \pm 0.0005 \pm 0.0017$
Γ_{+-}/Γ_{Ke3}	83725/(979799 $\times$ 8)	0.265/ 0.121	$(4.856 \pm 0.017 \pm 0.023) \times 10^{-3}$
Γ_{00}/Γ_{000}	100365/(1609324 $\times$ 5)	0.150/ 0.054	$(4.446 \pm 0.016 \pm 0.019) \times 10^{-3}$

TABLE V: Total uncertainties and correlation coefficients for the partial width ratios.

	$\Gamma_{K\mu3}/\ \Gamma_{Ke3}$	$\Gamma_{000}/\ \Gamma_{Ke3}$	$\Gamma_{+-0}/\ \Gamma_{Ke3}$	$\Gamma_{+-}/\ \Gamma_{Ke3}$	$\Gamma_{00}/\ \Gamma_{000}$
Total Error	0.0026	0.0055	0.0018	0.029×10^{-3}	0.025×10^{-3}
			Correlation coefficients		
$\Gamma_{K\mu3}/\ \Gamma_{Ke3}$	1.00				
$\Gamma_{000}/\ \Gamma_{Ke3}$	0.14	1.00			
$\Gamma_{+-0}/\ \Gamma_{Ke3}$	0.21	-0.06	1.00		
$\Gamma_{+-}/\ \Gamma_{Ke3}$	0.24	-0.07	0.49	1.00	
$\Gamma_{00}/\ \Gamma_{000}$	0.09	0.30	0.04	0.07	1.00

TABLE VI: K_L branching fractions and partial widths (Γ_i). The partial width measurements use the PDG average for the K_L lifetime: $\tau_L = (5.15 \pm 0.04) \times 10^{-8}$ sec [2]. The quoted errors are the sum in quadrature of statistical and systematic uncertainties.

Decay Mode	Branching Fraction	Γ_i ($10^7 s^{-1}$)
$K_L \to \pi^{\pm}e^{\mp}\nu$	0.4067 ± 0.0011	0.7897 ± 0.0065
$K_L \to \pi^{\pm}\mu^{\mp}\nu$	0.2701 ± 0.0009	0.5244 ± 0.0044
$K_L \to \pi^{+}\pi^{-}\pi^{0}$	0.1252 ± 0.0007	0.2431 ± 0.0023
$K_L \to \pi^{0}\pi^{0}\pi^{0}$	0.1945 ± 0.0018	0.3777 ± 0.0045
$K_L \to \pi^{+}\pi^{-}$	$(1.975 \pm 0.012) \times 10^{-3}$	$(3.835 \pm 0.038) \times 10^{-3}$
$K_L \to \pi^{0}\pi^{0}$	$(0.865 \pm 0.010) \times 10^{-3}$	$(1.679 \pm 0.024) \times 10^{-3}$

$\tau_L = (5.15 \pm 0.04) \times 10^{-8}$ sec, these branching fractions correspond to the partial widths quoted in the same table.

The $K_L \to \pi\pi$ measurements, combined with the kaon lifetimes, also provide a precise measurement of $|\eta_{+-}|^2 \equiv \Gamma(K_L \to \pi^+\pi^-)/\Gamma(K_S \to \pi^+\pi^-)$:

$$|\eta_{+-}|^2 = \frac{\tau_S}{\tau_L}\frac{B^L_{\pi^+\pi^-} + B^L_{\pi^0\pi^0}[1 + 6Re(\epsilon'/\epsilon)]}{1 - B^S_{\pi\ell\nu}}, \qquad (10)$$

where $B^L_{\pi^+\pi^-}$ and $B^L_{\pi^0\pi^0}$ are the $K_L \to \pi\pi$ branching fractions quoted in Table VI, $\tau_S = (0.8963 \pm 0.0005) \times 10^{-10}$ sec [51], and $Re(\epsilon'/\epsilon) = (16.7 \pm 2.3) \times 10^{-4}$ [1, 2, 7]. We calculate the $K_S \to \pi\ell\nu$ branching fraction $B^S_{\pi\ell\nu} = 0.118\%$ assuming that $\Gamma(K_S \to \pi\ell\nu) = \Gamma(K_L \to \pi\ell\nu)$. The resulting value of $|\eta_{+-}|$ is

$$|\eta_{+-}| = (2.228 \pm 0.010) \times 10^{-3}. \qquad (11)$$

The uncertainty in τ_L contributes 0.009×10^{-3} to the uncertainty in $|\eta_{+-}|$ while our $K_L \to \pi\pi$ branching fraction measurements contribute an uncertainty of 0.005×10^{-3}; τ_S and $Re(\epsilon'/\epsilon)$ contribute negligibly to the error in $|\eta_{+-}|$.

IX. COMPARISON WITH PREVIOUS PARTIAL WIDTH AND $|\eta_{+-}|$ MEASUREMENTS

The new KTeV measurements of the partial width ratios and K_L branching fractions are on average a factor of two more precise than the current world average values, but are not in good agreement with these averages. Figure 15 shows a comparison of the KTeV and PDG values for the five partial width ratios. Of the five partial width ratios, only the Γ_{00}/Γ_{000} measurement is in good agreement; note that Γ_{00}/Γ_{000} is the only ratio that does not include the $K_L \to \pi^{\pm}e^{\mp}\nu$ decay mode. Our measurements of $\Gamma_{K\mu3}/\Gamma_{Ke3}$ and $\Gamma_{+-0}/\Gamma_{Ke3}$ disagree with the PDG by 5%, and our measurements of $\Gamma_{000}/\Gamma_{Ke3}$ and Γ_{+-}/Γ_{Ke3} disagree with the PDG by 10%. Figure 16 shows the corresponding comparison of KTeV and PDG branching fractions. The discrepancies between KTeV and the PDG can be reduced significantly by applying a 7% relative shift to either the KTeV or PDG values for B($K_L \to \pi^{\pm}e^{\mp}\nu$).

Another measurement, which has not yet been included in the PDG summary, is the KLOE measurement of $R^{\pi}_S = \Gamma(K_S \to \pi^+\pi^-)/\Gamma(K_S \to \pi^0\pi^0) = 2.236 \pm 0.015$ [8]. The KTeV measurements of $B(K_L \to \pi^+\pi^-)$ and $B(K_L \to \pi^0\pi^0)$, along with the world average value of $Re(\epsilon'/\epsilon)$, give $R^{\pi}_S = 2.261 \pm 0.033$ in good agreement with, but less precise than, the KLOE result.

To understand the discrepancy between KTeV and the PDG averages, we have considered the 49 measurements and fit results used in the PDG averages [2]. 34 of

TABLE VII: Total uncertainties and correlation coefficients for the K_L branching ratios.

	B($K_L \to \pi^\pm e^\mp \nu$)	B($K_L \to \pi^\pm \mu^\mp \nu$)	B($K_L \to \pi^0\pi^0\pi^0$)	B($K_L \to \pi^+\pi^-\pi^0$)	B($K_L \to \pi^+\pi^-$)	B($K_L \to \pi^0\pi^0$)
Total Error	0.0011	0.0009	0.0018	0.0007	0.012×10^{-3}	0.010×10^{-3}
			Correlation coefficients			
$B(K_L \to \pi^\pm e^\mp \nu)$	1.00					
$B(K_L \to \pi^\pm \mu^\mp \nu)$	0.15	1.00				
$B(K_L \to \pi^0\pi^0\pi^0)$	-0.77	-0.62	1.00			
$B(K_L \to \pi^+\pi^-\pi^0)$	0.18	0.08	-0.54	1.00		
$B(K_L \to \pi^+\pi^-)$	0.28	0.22	-0.48	0.49	1.00	
$B(K_L \to \pi^0\pi^0)$	-0.72	-0.54	0.89	-0.46	-0.39	1.00

these measurements involve decay modes with branching fractions greater than 1%. Figure 17 shows the distribution of residuals (normalized by uncertainty) between these measurements and values obtained using the new KTeV measurements. The χ^2 per degree of freedom is 82.9/34 showing a clear inconsistency. Approximately 40 units of the χ^2 come from the three measurements with greater than 3σ disagreement with KTeV: the measurement of $\Gamma_{K\mu3}/\Gamma_{Ke3}$ reported by Cho 80 [9], and the measurements of Γ_{000} and $\Gamma_{+-0}/\Gamma_{Ke3}$ from NA31 [10]. It is interesting to note that in the same paper, NA31 reports $\Gamma_{000}/\Gamma_{+-0} = 1.611 \pm 0.037$, not involving the $K_L \to \pi^\pm e^\mp \nu$ decay mode, which is consistent with KTeV's measurement of $\Gamma_{000}/\Gamma_{+-0} = 1.567 \pm 0.020$; this NA31 measurement is not used in the PDG branching ratio fit because it is not independent of the other NA31 measurements included in the fit.

Figure 18 compares our new determination of $|\eta_{+-}|$ with the two measurements based on K_L-K_S interference [52]. The average of these two previous measurements gives $|\eta_{+-}| = (2.295 \pm 0.025) \times 10^{-3}$, which disagrees with the KTeV evaluation by 2.7σ. Figure 18 also shows $|\eta_{+-}|$ determined from the charge asymmetry assuming CPT invariance [53]; the value is consistent with all other measurements.

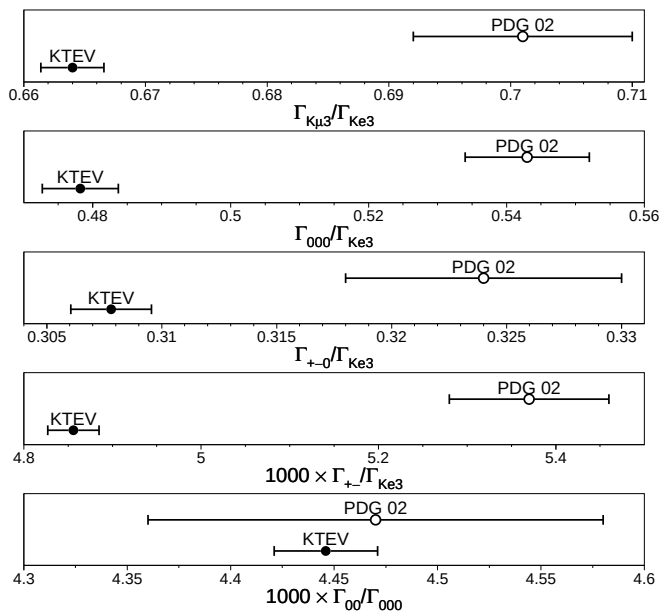

FIG. 15: Partial width ratios measured by KTeV (dots) and from PDG fit (open circles).

X. CONCLUSIONS

In summary, we have measured the branching fractions for the six K_L decay modes with branching fractions greater than 0.05%. The new measurements are about a factor of two more precise than current world averages, but are not in good agreement with these averages. Compared to the PDG fit [2], the KTeV measurement of $B(K_L \to \pi^\pm e^\mp \nu)$ is higher by 5%, $B(K_L \to \pi^0\pi^0\pi^0)$ is lower by 8%, $B(K_L \to \pi^+\pi^-)$ is lower by 5%, and $B(K_L \to \pi^0\pi^0)$ is lower by 8%. Our measurements of $B(K_L \to \pi^\pm \mu^\mp \nu)$ and $B(K_L \to \pi^+\pi^-\pi^0)$ are consistent with the PDG fit.

The new K_L branching fractions will require the adjustment of several rare K_L branching fractions for which the main K_L decay modes are used as normalization. The K_L branching fraction measurements also may be used to determine several parameters, including $|\eta_{+-}| = (2.228 \pm 0.010) \times 10^{-3}$, reported in this paper, and $|V_{us}|$, described in [39].

XI. ACKNOWLEDGMENTS

We gratefully acknowledge the support and effort of the Fermilab staff and the technical staffs of the participating institutions for their vital contributions. This work was supported in part by the U.S. Department of Energy, The National Science Foundation, and The Ministry of Education and Science of Japan.

APPENDIX A: DETERMINATION OF TRACKING LOSSES

The determination of the absolute track reconstruction efficiency is most important for the measurement

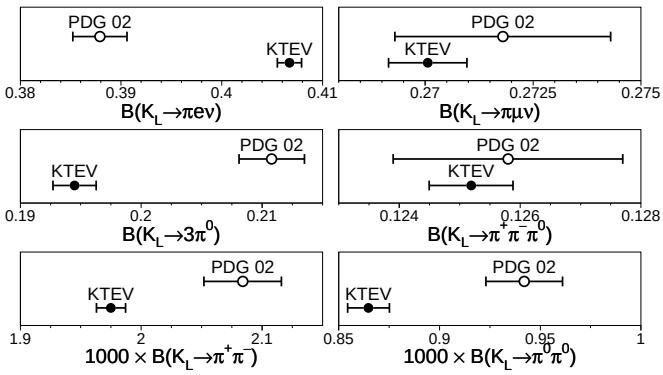

FIG. 16: K_L branching fractions measured by KTeV (dots) and from PDG fit (open circles).

of $\Gamma_{000}/\Gamma_{Ke3}$ which compares a decay mode with two charged tracks to a mode without charged particles in the final state. The causes of tracking loss fall into four categories: (i) missing or corrupted hits induced by accidental activity, δ-rays, and non-Gaussian tails in the chamber response; (ii) many spurious hits, mainly from accidental activity, which confuse pattern recognition; (iii) failure of track segments to satisfy matching criteria at the analysis magnet or decay vertex because of large angle scattering and $\pi \to \mu\nu$ decays; (iv) hadronic interactions in the spectrometer. All of these effects are included in the Monte Carlo simulation, as described in [1]. Pion decay is the main source of track loss, and is well described in the MC. This appendix describes an inclusive study of all other sources of track loss. The first three sources of track loss are related to the drift chamber performance, and are described in Sec. A 1. The effect of hadronic interactions is described in Sec. A 2.

The measurement of the tracking loss is based on partially reconstructed $K_L \to \pi^+\pi^-\pi^0$ decays that are identified by the $\pi^0 \to \gamma\gamma$ decay along with one or two additional hadronic clusters in the CsI calorimeter (i.e, clusters with transverse profile inconsistent with a photon). Ideally, $K_L \to \pi^+\pi^-\pi^0$ decays could be cleanly identified using only the four clusters in the CsI calorimeter, leading to a direct measurement of the two-track inefficiency; unfortunately, this sample has significant background. To obtain a $K_L \to \pi^+\pi^-\pi^0$ sample with low enough background for this study, we also require either a completely reconstructed pion track or some reconstructed track segments. With this partial reconstruction, the missing track information can be predicted from kinematic constraints, and then compared with the track information found by the track reconstruction. The data used for this study were collected in a trigger that requires energy in the CsI calorimeter and rejects events with activity in the muon system.

The two-track inefficiency is measured in two steps. First, we measure the single track inefficiency after one track is reconstructed (η_1). Next, we measure the probability of finding exactly zero tracks (η_0). The corresponding two-track loss, η_2, is then given by $2\eta_1 + \eta_0$.

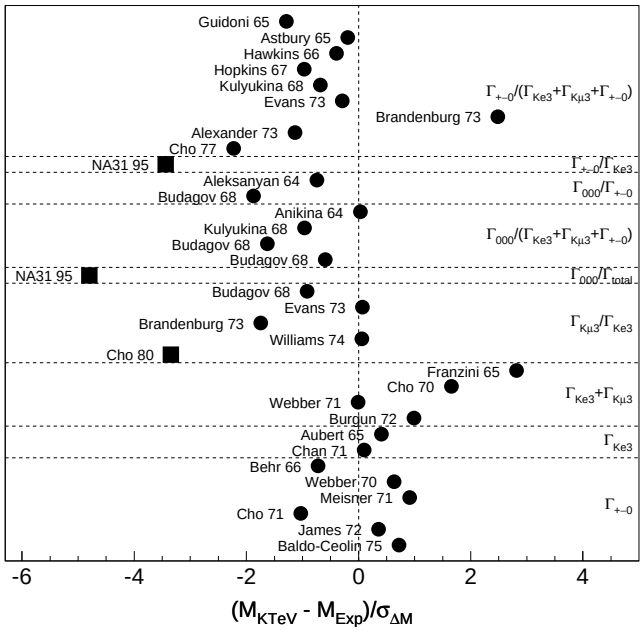

FIG. 17: Residual distribution between 34 individual measurements (M_{Exp}) used in the PDG fit and the KTeV determinations of these quantities (M_{KTeV}). $\sigma_{\Delta M}$ is the uncertainty on $M_{KTeV} - M_{Exp}$. Measurements disagreeing with KTeV by more than 3σ are shown as solid squares. The measurements are **Guidoni 65** [11], **Astbury 65** [12], **Hawkins 66** [13], **Hopkins 67** [14], **Kulyukina 68** [15], **Evans 73** [16], **Brandenburg 73** [17], **Alexander 73** [18], **Cho 77** [19], **NA31 95** [10], **Aleksanyan 64** [20], **Budagov 68** [21], **Anikina 64** [22], **Williams 74** [23], **Cho 80** [9], **Franzini 65** [24], **Cho 70** [25], **Webber 71** [26], **Burgun 72** [27], **Aubert 65** [28], **Chan 71** [29], **Behr 66** [30], **Webber 70** [31], **Meisner 71** [32], **Cho 71** [33], **James 72** [34], **Baldo-Ceolin 75** [35],

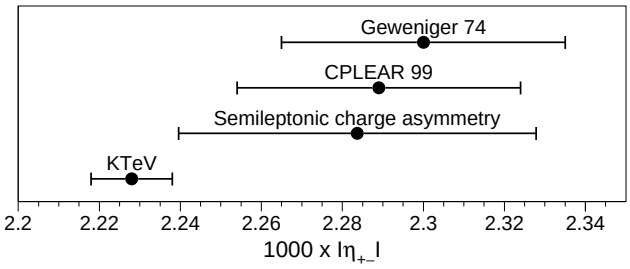

FIG. 18: Comparison of KTeV's $|\eta_{+-}|$ measurement with previous measurements based on K_L-K_S interference [36, 37], and the semileptonic charge asymmetry [2, 38]. Note that the CPLEAR value of $|\eta_{+-}|$ has been adjusted to $\tau_S = 0.8963 \times 10^{-10}$ sec using their quoted dependence on the K_S lifetime.

1. Tracking Inefficiency

The study of the single track efficiency uses events with a reconstructed $\pi^0 \to \gamma\gamma$ along with two hadronic clusters in the CsI calorimeter. Requiring exactly two hadronic clusters suppresses $K_L \to \pi^+\pi^-\pi^0$ decays with hadronic interactions in the spectrometer because such events tend to create additional hadronic clusters. Events with $\pi \to \mu\nu$ decays are also suppressed because these events leave only one hadron cluster. One of the two hadron clusters must be matched to a fully reconstructed track in the spectrometer, leaving two possible kinematic solutions for the missing track. The fully reconstructed track, along with the measured position of the other hadron cluster (associated with the missing track), provides sufficient information to select the correct kinematic solution for the missing pion trajectory. Figure 19 illustrates this selection. For the high intensity sample, we find the single track inefficiency (η_1) to be $(1.47 \pm 0.02)\%$ in data and $(1.32 \pm 0.02)\%$ in MC; in the low intensity sample, $\eta_1 = (0.18 \pm 0.02)\%$ in data and $(0.13 \pm 0.02)\%$ in MC.

In the above study, the reconstructed track requirement excludes the case in which correlated hit losses within a single drift chamber result in no reconstructed tracks. To account for correlated losses within a drift chamber, we perform a separate analysis to measure the fraction of events with zero reconstructed tracks (η_0). We start with the same calorimeter selection of two photon clusters for $\pi^0 \to \gamma\gamma$ and two hadron clusters. Next, we require two reconstructed track segments, either both upstream of the analysis magnet in DC1 and DC2, or both downstream of the analysis magnet in DC3 and DC4. Figure 20 shows the $\pi^+\pi^-\pi^0$ invariant mass distributions for these two samples. The $\pi^+\pi^-\pi^0$-mass resolution for the DC1-DC2 (DC3-DC4) selection is about 3 MeV/c^2 (2 MeV/c^2) compared to 1 MeV/c^2 for the standard reconstruction. The tails are well described by the $K_L \to \pi^+\pi^-\pi^0$ MC. For the high intensity sample, we find $\eta_0 = (0.35 \pm 0.02)\%$ in data and $(0.06 \pm 0.02)\%$ in MC. For the low intensity sample, $\eta_0 = (0.03 \pm 0.01)\%$ in data and zero in MC.

In the analyses for both η_1 and η_0, we ensure that the special selection does not introduce biases in the tracking efficiency, and that the efficiency corrections are applicable for the nominal selection of charged decay modes. One of the most important aspects in the tracking inefficiency study is to require separation between the reconstructed track (or track segment) and the kinematically predicted track (or track segment). This requirement is necessary because nearby tracks have a large tracking inefficiency, which is irrelevant for the nominal analysis that uses the track separation cut. Figure 21 shows η_1 as a function of X-separation (ΔX) between the two tracks at DC1. At small track separation, the inefficiency is larger than 20%. A requirement of $\Delta X > 7$ cm safely removes tracks with small separation.

The total two-track inefficiency ($\eta_2 = 2\eta_1 + \eta_0$) depends strongly on beam intensity. For the high intensity period, $\eta_2 = (3.28 \pm 0.04)\%$ in data; it is not completely reproduced by the simulation for which $\eta_2 = (2.70 \pm 0.05)\%$. For the low intensity period, the inefficiency in data is much smaller, $(0.38 \pm 0.06)\%$; the MC inefficiency is $(0.26 \pm 0.05)\%$, which agrees with the data. Based on these measurements, we apply a -0.6% correction to the acceptance for the high intensity period and a -0.12% correction for the low intensity period. The uncertainty on this correction is taken as 100% of the effect: 0.6% and 0.12% for the high and low intensity periods, respectively.

2. Hadronic Interactions in the Spectrometer

From our Monte Carlo simulation, the track loss from hadronic interactions in the spectrometer is 0.7% per pion track. Since these interactions also cause the CsI cluster associated with the track to be lost, we cannot measure the track loss using the method described in Sec. A 1. To identify hadronic interactions clearly without the second pion cluster, we tag pions with an interaction between DC3 and DC4. We use partially reconstructed $K_L \to \pi^+\pi^-\pi^0$ decays using $\pi^0 \to \gamma\gamma$, one complete pion track, and hits from the second pion track in the first three drift chambers. Note that only one hadronic cluster, associated with the complete track, is required.

This study uses low intensity data for which the tracking inefficiency has a small effect. Events are vetoed if there are extra hits in any of the first three drift chambers; this further suppresses accidental activity and sim-

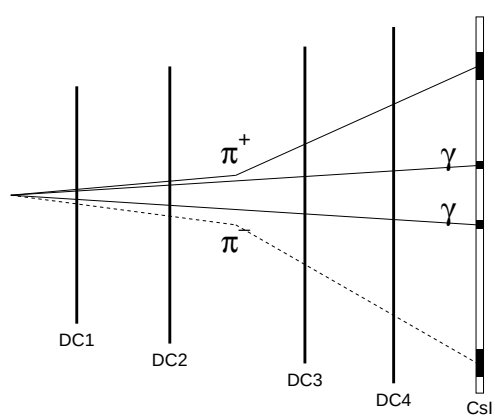

FIG. 19: $K_L \to \pi^+\pi^-\pi^0$ topology used to measure single track inefficiency (Z-X projection). Solid lines represent particles reconstructed in the detector. The dashed line indicates the pion trajectory calculated by the kinematics of the reconstructed particles with the assumption of a $K_L \to \pi^+\pi^-\pi^0$ decay.

plifies the particle trajectory determination. Hadronic interactions are tagged by requiring no hit in the last drift chamber within 1 cm of the second track extrapolation; according to MC, 90% of these events are due to a hadronic interaction. In data, (0.14±0.02)% of events are tagged as having hadronic interactions; the corresponding fraction for MC is $(0.096 \pm 0.005)\%$. The difference between these two fractions leads to a 50% uncertainty on the track loss from hadronic interactions.

APPENDIX B: TAILS IN THE CSI ENERGY RESPONSE

To measure the partial width ratios, it is important to understand tails in the CsI energy response for the four different types of particles detected in the analysis: electrons, photons, pions, and muons. The energy response tails affect the absolute detection efficiency, as well as particle misidentification that leads to background. In this appendix, we describe these tails, how they are determined from data, and how they are simulated.

KTeV's GEANT-based MC does not include the effects of photo-nuclear interactions (γN). If a γN reaction occurs during the electromagnetic shower development, a neutron or charged pion can escape the calorimeter, resulting in an energy deposit that is too low. Imperfections in the treatment of dead material (wrapping) between crystals also can lead to energy tails that are not properly modeled. These effects are empirically modeled and included in the MC by fitting a function to the low-side tail in the electron E/p distribution (Fig. 2(a)). The key point in this procedure is to select a sample of $K_L \to \pi^\pm e^\mp \nu$ decays with low enough background to avoid pion contamination for electron E/p values as low as 0.6. To achieve such electron purity, the pion is required to satisfy $E/p < 0.3$ to avoid swapping the electron and pion assignments, and $m_{\pi\pi} > 0.370$ GeV/c^2 to reject background from $K_L \to \pi^+\pi^-\pi^0$ decays. $K_L \to \pi^\pm\mu^\mp\nu$ decays are vetoed by the muon system. With the nominal electron selection requirement of $E/p > 0.92$, the inefficiency is measured to be 0.2%. This non-Gaussian tail also affects photons in the neutral decay modes; the presence of this tail changes the $K_L \to \pi^0\pi^0\pi^0$ acceptance by 0.7%.

The electron E/p tail in Fig. 2(a) shows losses up to 40% of the incident energy (i.e., down to $E/p \sim 0.6$). To check for anomalous energy losses of more than 40%, we use a sample of muons collected in dedicated runs as explained in [1]. We select muons that are at least 3 mm away from any crystal boundary to avoid the known effects of the small amount of dead material (wrapping) between crystals. Figure 22 shows the energy deposit distribution for 5.5 million muons hitting the CsI calorimeter away from crystal boundaries. The fraction of events with an anomalously low energy deposit (below 200 MeV) is 5×10^{-5} in data; this effect is negligible in the branching fraction analysis.

For charged pions in the CsI calorimeter, the E/p distributions for data and GEANT-based MC agree reasonable well (Fig. 2(b)). The pion E/p cut inefficiency is measured in both data and MC with $K_L \to \pi^+\pi^-\pi^0$ decays in the low intensity sample. Note that with the full reconstruction of $K_L \to \pi^+\pi^-\pi^0$, the pion E/p cut is not needed to achieve a negligible background. The inefficiency difference between data and MC is measured as a function of the E/p requirement and the proximity to the beam holes. The data-MC inefficiency difference varies between 0.1% and 0.3%, and is used to correct the MC samples.

In the $K_L \to \pi^\pm\mu^\mp\nu$ analysis, at least one track is required to deposit less than 2 GeV in the CsI calorimeter

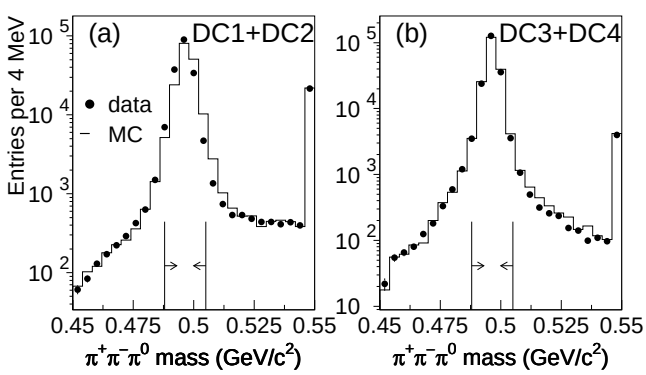

FIG. 20: For η_0 tracking inefficiency study, $\pi^+\pi^-\pi^0$ invariant mass distributions after all analysis requirements except $\pi^+\pi^-\pi^0$-mass. The data are shown as dots and the MC as a histogram. Distributions are based on identifying track segments in (a) DC1+DC2 and (b) DC3+DC4. Events with invariant mass above 0.55 GeV/c^2 are shown in the last bin. The horizontal arrows indicate the region selected by the $\pi^+\pi^-\pi^0$ mass requirement. The rightmost bin shows all events with mass greater than 0.55 GeV/c^2.

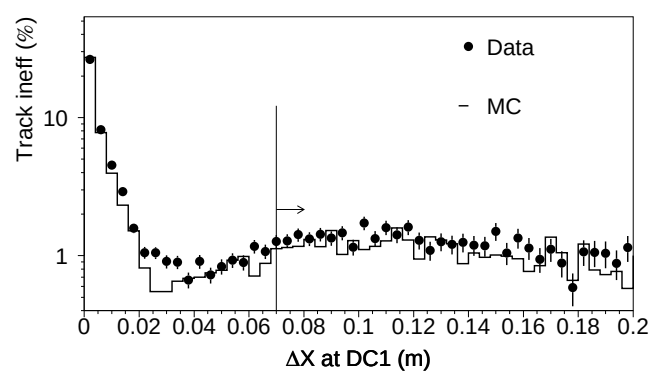

FIG. 21: Single track reconstruction inefficiency (η_1) as a function of the X-distance (ΔX) between the reconstructed track and the calculated track at DC1. The arrow indicates the selection requirement.

(i.e., less than 5 times the energy deposit of a minimum ionizing particle). In a separate $K_{\mu 3}$ analysis that identifies the muon with the muon hodoscope, the inefficiency of this cluster energy requirement is measured to be 0.3% in both data and MC. No correction is used to simulate the muon energy response in the CsI calorimeter.

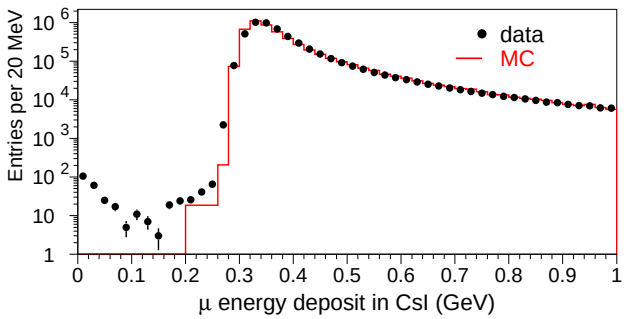

FIG. 22: Energy deposit in the CsI for muons with track projection at the CsI at least 3 mm from any crystal boundary. The data are shown as dots and the MC as a histogram.

[1] A. Alavi-Harati et al. (KTeV), Phys. Rev. **D67**, 012005 (2003), hep-ex/0208007.
[2] Particle Data Group, Phys. Ref. D **66**, 1 (2002).
[3] T. Alexopoulos et al. (KTeV) (2004), submitted to Phys. Rev. D, hep-ex/0406003.
[4] T. Andre (2004), to be submitted to Phys. Rev. D, hep-ph/0406006.
[5] E. Barberio and Z. Was, Comput. Phys. Commun. **79**, 291 (1994).
[6] R. Brun et al. (1994), GEANT 3.21, CERN, Geneva.
[7] J. R. Batley et al. (NA48), Phys. Lett. **B544**, 97 (2002), hep-ex/0208009.
[8] A. Aloiso et al. (KLOE), Phys. Lett. **B538**, 21 (2002).
[9] Y. Cho et al., Phys. Rev. **D22**, 2688 (1980).
[10] A. Kreutz et al., Z. Phys. **C65**, 67 (1995).
[11] P. Guidoni et al., Argonne Conf. p. 49 (1965).
[12] P. Astbury et al., Phys. Lett. **18**, 175 (1965).
[13] C. Hawkins, Phys. Lett. **21**, 238 (1966).
[14] F. E. H.W.K. Hopkins, T.C. Bacon, Phys. Rev. Lett. **19**, 185 (1967).
[15] L. Kulyukina et al., J. of Exp. and Theor. Phys. Lett. **26**, 20 (1968).
[16] G. Evans et al., Phys. Rev. **D7**, 36 (1973).
[17] G. Brandenburg et al., Phys. Rev. **D8**, 1978 (1973).
[18] G. Alexander et al., Nucl. Phys. **B65**, 301 (1973).
[19] Y. Cho et al., Phys. Rev. **D15**, 587 (1977).
[20] A. Aleksanyan et al., Dubna Conf. **2**, 102 (1964).
[21] I. Budagov et al., Nuovo Cim. **57A**, 182 (1968).
[22] M. Anikina et al., J. of Exp. and Theor. Phys. Lett. **19**, 42 (1964).
[23] H. Williams et al., Phys. Rev. Lett. **33**, 240 (1974).
[24] P. Franzini et al., Phys. Rev. **140B**, 127 (1965).
[25] Y. Cho et al., Phys. Rev. **D1**, 1970 (3031).
[26] B. Webber et al., Phys. Rev. **D3**, 64 (1971).
[27] G. Burgun et al., Nucl. Phys. **50**, 194 (1972).
[28] B. Aubert et al., Phys. Lett. **17**, 59 (1965).
[29] J. Chan, Thesis LBL **350** (1971).
[30] L. Behr et al., Phys. Lett. **22**, 540 (1966).
[31] B. Webber et al., Phys. Rev. **D1**, 1967 (1970).
[32] G. Meisner et al., Phys. Rev. **D3**, 59 (1971).
[33] Y. Cho et al., Phys. Rev. **D3**, 1557 (1971).
[34] F. James et al., Nucl. Phys. **B49**, 1 (1972).
[35] M. Baldo-Ceolin et al., Nuovo Cim. **25A**, 688 (1975).
[36] C. Geweniger et al., Phys. Lett. **48B**, 487 (1974).
[37] A. Apostolakis et al., Phys. Lett. **B458**, 545 (1999).
[38] A. Alavi-Harati et al., Phys. Rev. Lett. **88**, 181601 (2000).
[39] T. Alexopoulos et al. (KTeV) (2004), submitted to Phys. Rev. Lett., hep-ex/0406001.
[40] The contribution of rare decays to the K_L total width is mostly from $B(K_L \to \gamma\gamma) = 0.060\%$, $B(K_L \to \pi^0\pi^\pm e^\mp \nu) = 0.005\%$, and the direct emission $B(K_L \to \pi^+\pi^-\gamma) = 0.002\%$ [2]. The invisible width is assumed to be zero.
[41] $\Gamma_{K\mu 3}/\Gamma_{Ke3}$ has poor statistics in the high intensity sample because the only trigger which does not veto muons was pre-scaled by 10,000.
[42] For the decay modes with branching fractions greater than 10% (semileptonic and 3π), even the relaxed, highly prescaled triggers have high statistics. To get sufficient statistics in the $K \to \pi\pi$ modes (with $BR \sim 0.1\%$), we use the same 2-pion triggers as in the ϵ'/ϵ analysis. For Γ_{+-}/Γ_{Ke3}, we use the standard Level 1 and Level 2 trigger, but use the pre-scaled (1/100) sample in which there is no Level 3. For Γ_{00}/Γ_{000}, we use 5% of the nominal sample in the ϵ'/ϵ analysis.
[43] The measurement of Γ_{00}/Γ_{000} is the only partial width ratio based on data from two different triggers. This analysis uses the same four and six cluster triggers used in the ϵ'/ϵ analysis. For the low intensity sample, used as a

crosscheck, both decay modes are collected with the same neutral-mode minimum bias trigger, but the low number of $K_L \to \pi^0\pi^0$ events in this sample limits the precision of the measurement.

[44] `RING` is defined as the area, in cm^2, of the smallest square centered on the beam that contains the transverse decay vertex at the Z position of the CsI calorimeter. For all-neutral events, `RING` is defined in terms of the center-of-energy measured in the calorimeter [1].

[45] The background to $K_L \to \pi^+\pi^-$ is 0.16%, which is larger than the 0.1% background quoted in [1]; this is because the pion selection efficiency does not cancel in Γ_{+-}/Γ_{Ke3}, and therefore the E/p requirement is relaxed to reduce the systematic uncertainty.

[46] In the ϵ'/ϵ analysis, the $\chi^2_{\pi^0}$ cuts are 12 (24) for $K_L \to \pi^0\pi^0$ ($K_L \to \pi^0\pi^0\pi^0$). To measure partial width ratios with a different number of neutral pions in the numerator and denominator, this $\chi^2_{\pi^0}$ requirement is relaxed to reduce acceptance uncertainties.

[47] The 0.32% $\pi^0\pi^0\pi^0$ background in the $K_L \to \pi^0\pi^0$ sample is three times larger than in the ϵ'/ϵ analysis [1] because of the much looser $\chi^2_{\pi^0}$ cut.

[48] For $K_L \to \pi^+\pi^-\pi^0$, the acceptance and yield are calculated in five independent $m_{\pi\pi}$ bins (20 MeV/c^2 per bin), and then summed for the measurement of $\Gamma_{+-0}/\Gamma_{Ke3}$; this reduces sensitivity to the decay form factors.

[49] The nominal $K_L \to \pi^0\pi^0\pi^0$ and $K_L \to \pi^0\pi^0$ analyses allow hits in the trigger hodoscope.

[50] For τ_L, we use the PDG average [2] rather than the PDG fit value to avoid correlations with K_L branching fractions.

[51] We use average τ_S from KTeV and NA48.

[52] We ignore the PDG fit for $|\eta_{+-}|$ because it uses the $K_L \to \pi\pi$ branching fractions. The disagreement of the KTeV and PDG values for these branching fractions has already been discussed.

[53] $|\eta_{+-}|$ is related to δ_ℓ, the $K_L \to \pi^\pm\ell^\mp\nu$ charge asymmetry: $|\eta_{+-}| = (0.5\,\delta_\ell/\cos\phi_{+-}) + |\epsilon'|$, where $\delta_\ell = (3307 \pm 64) \times 10^{-6}$ is the average of the recent KTeV measurement [38] and previous measurements [2], $\phi_{+-} = (43.51 \pm 006)^\circ$ is the superweak phase [2], and $|\epsilon'| = 3.8 \times 10^{-6}$ [2].